Atmospheric Sea Spray Modeling in the North-East Atlantic Ocean using Tunnel-Derived Generation Functions and the SUMOS Cruise Dataset

WIlliam Bruch[1], W Bruch[2,3,4], C Yohia[5], P Tulet[3], A Limoges[2], P Sutherland[6,7], A M J van Eijk[4,6,7,8], T Missamou[2], and J Piazzola[2,8]

[1]Affiliation not available
[2]UMR 7294), Mediterranean Institute of Oceanography (MIO, Université de Toulon
[3]Laboratoire d'Aérologie, UPS/CNRS
[4]Ecole Centrale de Nantes, LHEEA, CNRS (UMR 6598
[5]OSU-Pytheas, Aix-Marseille Université
[6]Univ. Brest
[7]Laboratoire d'Océanographie Physique et Spatiale (LOPS), CNRS, IUEM
[8]TNO

February 20, 2023

Abstract

This study contributes to the communal effort to improve understanding of sea spray generation and transport. For the first time, laboratory-derived sea spray generation functions (SSGFs) are parameterized in the Meso-NH mesoscale atmospheric model and are field tested. Formulated from the MATE19 laboratory experiments (Bruch et al., 2021) two SSGFs are driven by the upwind component of the wave-slope variance S2x (herein B21A), or both S2x and the wind friction velocity cubed u3* (herein B21B). As part of our first attempt to incorporate the SSGFs in Meso-NH, the simulations are run without a wave model, and the wave-wind SSGFs are assumed wind-dependent. Model evaluation is achieved with sea spray and meteorological measurements acquired over the 0.1-22.75 µm radius range and 1-20 m s-1 U10 wind speeds, 15 meters above the sea surface onboard R/V Atalante during the 25 day SUMOS field campaign in the Bay of Biscay. The B21B SSGF offers particularly good sensitivity to a wide range of environmental conditions over the size range, with an average overestimation by a factor 1.5 compared with measurements, well below the deviations reported elsewhere. B21A also performs well for larger droplets at wind speeds above 15 m s-1. Associated with airflow separation and wave breaking, the wave-slope variance proves to be a key parameter for the scaling of sea spray generation. Using model outputs obtained with B21B, sea spray can be found far beyond the marine atmospheric boundary layer, with large plumes reaching 100 km inland and altitudes of 2.5 km.

Plain Language Summary

The effects of sea spray on weather and climate remain poorly understood as a result of sparse measurements and large uncertainties in the generation flux. With the aim of improving sea spray transport in atmospheric models, two sea spray generation functions derived from the MATE19 laboratory campaign are parameterized in the Meso-NH mesoscale atmospheric model. The simulations are run over the Bay of Biscay in February-March 2021, and are compared with sea spray concentrations measured during the SUMOS field campaign. Results show that the laboratory-derived generation functions allow accurate predictions of sea spray concentrations. Furthermore, simulations show that sea spray droplets can be transported far over land, and high into the atmosphere.

Atmospheric Sea Spray Modeling in the North-East Atlantic Ocean using Tunnel-Derived Generation Functions and the SUMOS Cruise Dataset

W. Bruch[1,6*], C. Yohia[2], P. Tulet[3], A. Limoges[1], P. Sutherland[4], A. M. J. van Eijk[5,6], T. Missamou[1], J. Piazzola[1]

[1]Mediterranean Institute of Oceanography (MIO-UMR 7294), Université de Toulon, Toulon, France
[2]OSU-Pytheas, Aix-Marseille Université, Marseille, France
[3]Laboratoire d'Aérologie, UPS/CNRS, Toulouse, France
[4]Ifremer, Univ. Brest, CNRS, IRD, Laboratoire d'Océanographie Physique et Spatiale (LOPS), IUEM, Brest, France
[5]TNO, The Hague, Netherlands
[6]Ecole Centrale de Nantes, LHEEA, CNRS (UMR 6598), 44321 Nantes, France

Key Points:

- Wave-slope variance behavior is comparable in laboratory and field conditions, motivating the use of laboratory-derived SSGFs in the field.
- Parameterized with laboratory SSGFs and validated using field measurements, Meso-NH yields accurate sea spray concentrations.
- By populating the atmosphere beyond 2.5 km altitude and 100 km inland, sea spray can intervene in a range of weather and climate processes.

*1 Rue de la Noë, Nantes

Corresponding author: William Bruch, william.bruch@ec-nantes.fr

Abstract

This study contributes to the communal effort to improve understanding of sea spray generation and transport. For the first time, laboratory-derived sea spray generation functions (SSGFs) are parameterized in the Meso-NH mesoscale atmospheric model and are field tested. Formulated from the MATE19 laboratory experiments (Bruch et al., 2021) two SSGFs are driven by the upwind component of the wave-slope variance $\langle S_x^2 \rangle$ (herein B21A), or both $\langle S_x^2 \rangle$ and the wind friction velocity cubed u_*^3 (herein B21B). As part of our first attempt to incorporate the SSGFs in Meso-NH, the simulations are run without a wave model, and the wave-wind SSGFs are assumed wind-dependent. Model evaluation is achieved with sea spray and meteorological measurements acquired over the 0.1–22.75 µm radius range and 1–20 m s^{-1} U_{10} wind speeds, 15 meters above the sea surface onboard R/V Atalante during the 25 day SUMOS field campaign in the Bay of Biscay. The B21B SSGF offers particularly good sensitivity to a wide range of environmental conditions over the size range, with an average overestimation by a factor 1.5 compared with measurements, well below the deviations reported elsewhere. B21A also performs well for larger droplets at wind speeds above 15 m s^{-1}. Associated with airflow separation and wave breaking, the wave-slope variance proves to be a key parameter for the scaling of sea spray generation. Using model outputs obtained with B21B, sea spray can be found far beyond the marine atmospheric boundary layer, with large plumes reaching 100 km inland and altitudes of 2.5 km.

Plain Language Summary

The effects of sea spray on weather and climate remain poorly understood as a result of sparse measurements and large uncertainties in the generation flux. With the aim of improving sea spray transport in atmospheric models, two sea spray generation functions derived from the MATE19 laboratory campaign are parameterized in the Meso-NH mesoscale atmospheric model. The simulations are run over the Bay of Biscay in February–March 2021, and are compared with sea spray concentrations measured during the SUMOS field campaign. Results show that the laboratory-derived generation functions allow accurate predictions of sea spray concentrations. Furthermore, simulations show that sea spray droplets can be transported far over land, and high into the atmosphere.

1 Introduction

70% of Earth's surface is covered by oceans. Marine aerosols, generated from and above the ocean surface, represent a major component of the natural aerosol mass (Jaenicke, 1984; Yoon et al., 2007), and can dominate over the open ocean and the often densely populated coastal regions (Katoshevski et al., 1999; Sroka & Emanuel, 2021). Primary aerosols include aqueous-phase sea spray droplets (E. Monahan et al., 1982; Troitskaya et al., 2018) and sea salt particles. Emitted into the marine atmospheric boundary layer (MABL) from the ocean surface, film and jet droplets are associated with bubble bursting, generating particles that dominate the 1–15µm radius range for winds above 4 m s^{-1} at the height reference U_{10}, 10 meters above the mean water level (herein MWL). The larger spume droplets, born from surface-tearing mechanisms, are thought to dominate concentrations as well as the overall volume flux for horizontal wind speeds greater than 12 m s^{-1}.

Air-droplet dynamic and thermodynamic processes occur as sea spray is transported, mixed, and diffused in the highly turbulent atmospheric boundary layer. Sometimes referred to as a sandwich layer, sea spray can form a dense diphasic layer, damping the wave-wind momentum flux and saturating the surface drag (Lighthill, 1999;

Andreas, 2004; Fairall et al., 2009; Soloviev & Lukas, 2010; Rastigejev et al., 2011). Sea spray is also thought to modify air-sea enthalpy fluxes through droplet evaporation and temperature changes (Fairall et al., 1994; Richter & Sullivan, 2014; Rastigejev & Suslov, 2019), earning the name of evaporation layer. The range of feedbacks are of increasing interest for the understanding of extreme weather events, such as tropical cyclones, typhoons (Andreas, 1992; Andreas & Emanuel, 2001; Bao et al., 2011; B. Zhao et al., 2017), and heavy rainfall events (Ramanathan et al., 2001). Marine aerosols also constitute an important source of cloud condensation nucleii, which have been shown to play an important role in tropical cyclone development (Wang et al., 2014; Hoarau et al., 2018; Sroka & Emanuel, 2021) and to affect Earth's radiative budget (Jacobson, 2001; Boucher et al., 2013).

Significant predictive uncertainties remain for sea spray, with large deviations observed between commonly used emission schemes (de Leeuw et al., 2011; Tsyro et al., 2011; Chen et al., 2016; Neumann et al., 2016; Saliba et al., 2019). As a result, weather and climate effects of sea spray remain elusive. The environmental conditions required for the generation of spume droplets and the resulting consequences on the characteristics of the marine atmospheric boundary layer (MABL) remain poorly understood (Bianco et al., 2011; Veron et al., 2012; Veron, 2015; Lenain & Melville, 2017; Rogowski et al., 2021). To better understand their role in weather and climate, sea spray generation and transport in atmospheric numerical models must be improved.

Over the past three decades, sea spray generation functions (SSGFs) have gained in complexity. Often associated with wind speed alone (E. Monahan et al., 1986; Smith et al., 1993), sea spray generation has also been shown to depend on sea water composition (e.g. Mårtensson et al. (2003); Sellegri et al. (2006); Forestieri et al. (2018); Mehta et al. (2019)) and sea state (Iida et al., 1992; D. Zhao et al., 2006; Ovadnevaite et al., 2014; Laussac et al., 2018). The vast majority of wave-dependent SSGFs rely on peak wave parameters such as significant wave height (Ovadnevaite et al., 2014), wave age (Laussac et al., 2018), and wave steepness (Xu et al., 2021). Nevertheless, some studies suggest that the higher frequency end of the gravity wave spectrum represents a non-negligible and different contribution to the momentum, heat, gas and particle fluxes at the air-sea interface (Jähne & Riemer, 1990; Munk, 2009). The importance of considering different wave scales and complex surface geometry is illustrated in the laboratory study by Bruch et al. (2021) where the sea spray generation flux scales best with two formulations, one depending totally, and the other partially, on the upwind component of the multiscale wave-slope variance.

The omnidirectional wave-slope variance $\langle S^2_{x,y} \rangle$ is the sum of upwind (x direction) and crosswind (y direction) components so that $\langle S^2_{x,y} \rangle = \langle S^2_x \rangle + \langle S^2_y \rangle$. Long-studied in the remote sensing community for the estimation of the near-surface wind speed, $\langle S^2_{x,y} \rangle$ was found to be highly dependent on the local wind speed, especially at the smallest wavelengths, with which it is thought to have a linear (Cox & Munk, 1954; Bréon & Henriot, 2006) or a power law (Wu, 1972; Hauser et al., 2008) relationship. The wave-slope variance has also been used in other studies, such as to scale the form drag (Plant, 1982) or air-sea gas transfer velocities (Bock et al., 1999; Glover et al., 2007). Additionally, the slope of roughness elements on a surface is nondimensional and can be used to scale airflow separation at high Reynolds numbers, as is often the case at the ocean surface. The wave slope is also strongly related to wave breaking (e.g. Stokes (1880)). Both processes are key to sea spray generation, and have a limited dependence on element dimensions. Despite the different wave scales between the laboratory and the field, the SSGFs proposed by Bruch et al. (2021) may therefore be valid in real world conditions.

Present-day regional atmospheric models allow the transport of aerosols, but efforts are hindered for sea spray by significant uncertainties surrounding the generation flux. Measuring jet and spume droplet generation fluxes is a significant challenge in

the field. A solution is to take both SSGFs formulated by Bruch et al. (2021), and use them in real world conditions. In our study, we integrate the laboratory SSGFs in the mesoscale Meso-NH atmospheric model, and evaluate model performance using a new extensive and original dataset constructed during the SUMOS field campaign in the Bay of Biscay. The study is divided in three parts. Section 2 investigates the validity of laboratory upwind wave-slope variance $\langle S_x^2 \rangle$ in the field, and therefore of the laboratory SSGFs. Section 3 presents meteorological and sea spray measurements made during the SUMOS field campaign. Section 4 presents sea spray transport results using Meso-NH and the laboratory-derived SSGFs. Study results are discussed in Section 5. In the following, we demonstrate the potential of laboratory measurements by improving the accuracy of sea spray prediction in regional numerical models for jet and spume droplets. The Meso-NH model results are used to study the extent of jet and spume droplets over sea and land.

2 Using Laboratory $\langle S_x^2 \rangle$ in the Field

2.1 First Order Linearity of $\langle S_x^2 \rangle$ with Wind Speed

Bruch et al. (2021) reported sea spray fluxes derived from measurements conducted at the Sciences de l'Univers (OSU) Pytheas Institute large wave-wind interaction facility in Luminy (Marseille, France) during the MATE19 campaign. Two sea spray generation functions (SSGFs) were proposed. Both SSGFs have a 3–35 µm radius and 12–20 m s^{-1} wind speed validity range. They depend on two different non-dimensional numbers that describe wave-wind interaction, and inherently, the characteristics of the airflow in the marine atmospheric boundary layer (MABL). In this paper, we reserve the name B21A for the laboratory SSGF that depends on the upwind wave-slope variance component (denoted $\langle S_x^2 \rangle$) alone. The second SSGF, herein denoted B21B, depends on a non-dimension number P_S. P_S is written as a function of $\langle S_x^2 \rangle$ and the friction velocity cubed u_*^3:

$$P_S = \frac{u_*^3}{\nu_a g} \langle S_x^2 \rangle, \tag{1}$$

where ν_a is the viscosity of the ambient air, and g is the acceleration of gravity. This new nomenclature allows to better distinguish between the two SSGFs presented by Bruch et al. (2021).

We reuse the MATE19 (Bruch et al., 2021) wind and wave data, collected for five U_{10} wind speeds ranging 8-20 m s^{-1}, and four wave-types: one pure wind-wave case, and three monochromatic wave cases generated with a mechanical wavemaker. During MATE19, the wave-slope variance was obtained from differences in the water surface elevation, measured with an array of three wave gauges aligned with the general wind and wave direction, 10 mm apart, with a 256 Hz sampling frequency. Wave-slope variance estimates were computed with a cut-off wavelength of 20 mm, so as to focus on the complete gravity-driven wave spectrum. The laboratory $\langle S_x^2 \rangle$ thus encapsulates the gravity wave spectrum. Because of the orientation of the wave gauges, wave-slopes were only measured in the upwind direction, and crosswind components were therefore omitted. We also use data from a fifth wave type that was studied during the MATE19 campaign. This fifth wave type consists of a JONSWAP (Hasselmann et al., 1973) wave configuration, generated by the wavemaker (f_p=0.9 Hz for U_{10}=0 m s^{-1}), and exposed to the same 8–20 m s^{-1} U_{10} range as the other four wave types. These data were not included in Bruch et al. (2021) because the more complex wave type required longer meteorological, hydrodynamic and aerosol sampling durations, thus preventing to accurately estimate the vertical sea spray flux.

Historically (Cox & Munk, 1954) and in more recent studies (Bréon & Henriot, 2006; Lenain et al., 2019), authors generally consider a linear relationship between wind speed and the wave-slope variance. Figure 1 represents $\langle S_x^2 \rangle$ as a function of the U_{10} wind speed (cf. Fig. 1a) and the friction velocity u_* (cf. Fig. 1b), for the 5 wave types studied during MATE19. The linear functions (solid black lines) fit the laboratory measurements (black plus signs) well, with R^2=0.75 against U_{10}, and R^2=0.80 against u_*. At first order we confirm the linear relationship between $\langle S_x^2 \rangle$ and local wind speeds reported in the litterature. The linear regression function representing $\langle S_x^2 \rangle$ as a function of U_{10} (cf. Fig. 1a) is given by:

$$10^3 \langle S_x^2 \rangle = 3.48 \times U_{10} + 3.18 \pm c, \tag{2}$$

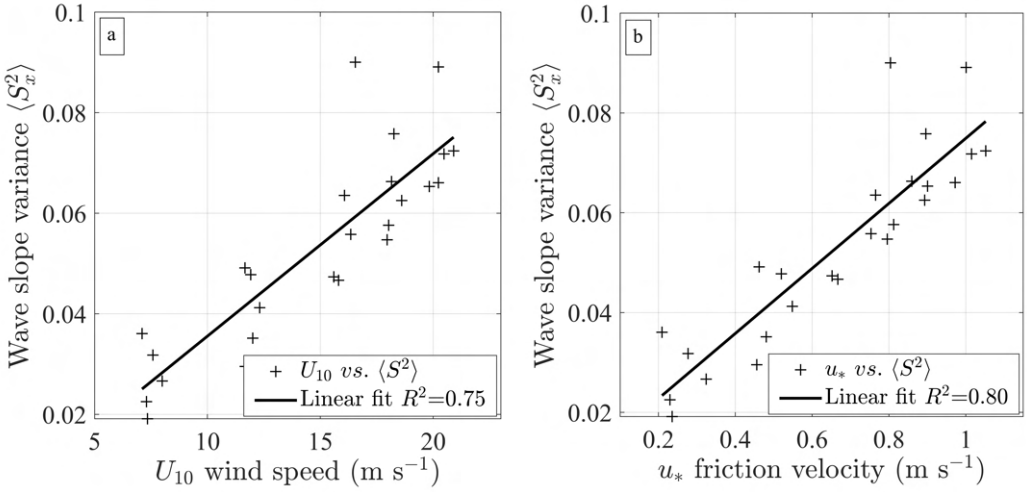

Figure 1. Wave-slope variance as a function of (a) wind speed U_{10} and (b) friction velocity u_* during MATE19. Laboratory data is represented by "+" signs. R^2 values correspond to the linear regression functions represented by black solid lines.

2.2 Comparing Laboratory $\langle S_x^2 \rangle$ with Real World Observations

The validity of both laboratory SSGFs in real world conditions heavily relies on whether the laboratory $\langle S_x^2 \rangle$, denoted $\langle S_{x-MATE19}^2 \rangle$ in the following, is representative of that observed in the field. One way of verifying this is to compare the overall linear relationship described by Eq. 2 (Sect. 2.1), with the formulations reported by Cox and Munk (1954) (denoted CM54) and Bréon and Henriot (2006) (denoted BH06) derived from airborne sun-glitter and satellite observations, respectively. The upwind CM54 and BH06 $\langle S_x^2 \rangle$ relationships with U_{10}, denoted $\langle S_{x-CM54}^2 \rangle$ and $\langle S_{x-BH06}^2 \rangle$ respectively, are presented in Fig. 2 (dashed and dotted lines, respectively). The solid line in Fig. 2 represents Eq. 2, i.e., the linear relationship derived from the MATE19 data. Both CM54 and BH06 assume linear relationships between $\langle S_{x,y}^2 \rangle$ and wind speed, and present very similar relationships. The slopes of the laboratory and remotely-sensed $\langle S_x^2 \rangle$ relationships with U_{10} are also very similar, but a bias exists. Compared with $\langle S_{x-CM54}^2 \rangle$, $\langle S_{x-MATE19}^2 \rangle$ values are 14% higher (0.0044 deviation) at 8 m s^{-1}, and

12.5% higher (0.007 deviation) at 16 m s^{-1}. This comparison yields similar results to other studies, with a 12% deviation reported between the wave model proposed by Elfouhaily et al. (1997), and $\langle S^2_{x,y-CM54} \rangle$ (Hauser et al., 2008). Considering the 10^{-3} offset between $\langle S^2_{x-MATE19} \rangle$ and $\langle S^2_{x-CM54} \rangle$ at $U_{10} = 0$, we can write:

$$\langle S^2_{x-MATE19} \rangle \approx 1.1 \times \langle S^2_{x-CM54} \rangle + 10^{-3}. \tag{3}$$

In addition to the first-order linear relationship between $\langle S^2_x \rangle$ and U_{10}, we observe a higher-order dependence of $\langle S^2_{x-MATE19} \rangle$ on the wave type. In Fig. 2, markers indicate the different wave types; wind waves ("□" symbols), JONSWAP spectra ("⋄" symbols), long waves ("○" symbols), intermediate waves ("△" symbols) and short waves ("▽" symbols). At each wind speed, the spread between the $\langle S^2_x \rangle$ values is consistently dependent on the different wave conditions tested during MATE19 (Bruch et al., 2021). The intermediate waves consistently lead to the highest $\langle S^2_x \rangle$ values and deviations from $\langle S^2_{x-CM54} \rangle$, followed by the short waves. $\langle S^2_{x-MATE19} \rangle$ values gradually decrease from the wind waves to the long waves, and ultimately the JONSWAP wave type. With the exception of the intermediate waves, the deviations between the different wave conditions tend to decrease for wind speeds approaching 20 m s^{-1}.

Good agreement between $\langle S^2_{x-MATE19} \rangle$ and $\langle S^2_{x-CM54} \rangle$ for laboratory wind waves (cf. Fig. 2, "□" symbol) despite the narrower wave spectra in the laboratory compared with the field. Earlier comparison between Cox and Munk (1954) and laboratory slope spectra was made by Plant (1982), who suggested that shorter fetch laboratory waves present higher slope densities and a higher dominant wave-slope for a limited frequency range, compared to the field. The higher laboratory slope density can therefore compensate for the narrowness of the slope spectrum. Furthermore, Wentz (1976) implies that CM54 represents the lower limit of wave-slope variance, and better represents windseas rather than large and lower frequency gravity waves. This is supported by the good resemblance between $\langle S^2_{x-CM54} \rangle$ and the wind wave condition in the present study (cf. Fig. 2), as well as comparable laboratory and field $\langle S^2_x \rangle$ ranges reported by Plant (1982) despite very different laboratory and field spectral peak frequencies.

We now consider the relatively large deviation between $\langle S^2_{x-MATE19} \rangle$ and $\langle S^2_{x-CM54} \rangle$ for short and intermediate waves. The wave-slope variance timeseries (with moving windows a few seconds wide – not shown here) show $\langle S^2_{x-MATE19} \rangle$ peaks at the wave crests, with higher values found for the most asymmetric and strongly breaking (Bruch et al., 2021) short and intermediate wave types. In contrast, the remote sensing techniques underlying the CM54 and NH06 formulations do not consider breaking events. In fact, Cox and Munk (1954) removed the wave breaking contribution to $\langle S^2_x \rangle$ for analysis. Therefore, the higher $\langle S^2_x \rangle$ values in Fig. 2 found for $\langle S^2_{x-MATE19} \rangle$ as compared to $\langle S^2_{x-CM54} \rangle$ and $\langle S^2_{x-NH06} \rangle$ may well be attributed to the contribution of breaking.

Alternatively, the overall 14% difference between MATE19 and CM54 may be partly caused by wave directionality. By nature, ocean waves show anisotropic behaviour. Wave-slope variance anisotropy is described by the ratio between the upwind and crosswind components $\gamma = \frac{\langle S^2_y \rangle}{\langle S^2_x \rangle}$. γ values reported by (Cox & Munk, 1954) in clean (no oil slick) water conditions approached 0.75 on average, reflecting relatively low anisotropy. More recent studies have suggested higher anisotropy in the field, with γ = 0.6-0.7 estimated by the omnidirectional wave model proposed by (Elfouhaily et al., 1997). It is not unlikely that the anisotropy in the Luminy tunnel (where the MATE19 data was collected) was even higher. However, if we recalculate the upwind $\langle S^2_{x-CM54} \rangle$ from the total omnidirection CM54 formulation with $\gamma = 0.66$, we obtain a surprisingly good fit with Eq. 2., as evidenced by the black dashed-dotted line labeled $\langle S^2_{x-MCM54} \rangle$ in Fig.2. Whilst this remains speculative, the general lack of comparable

laboratory and *in situ* measurements of wave-slope variance in the litterature hinders any deeper analysis.

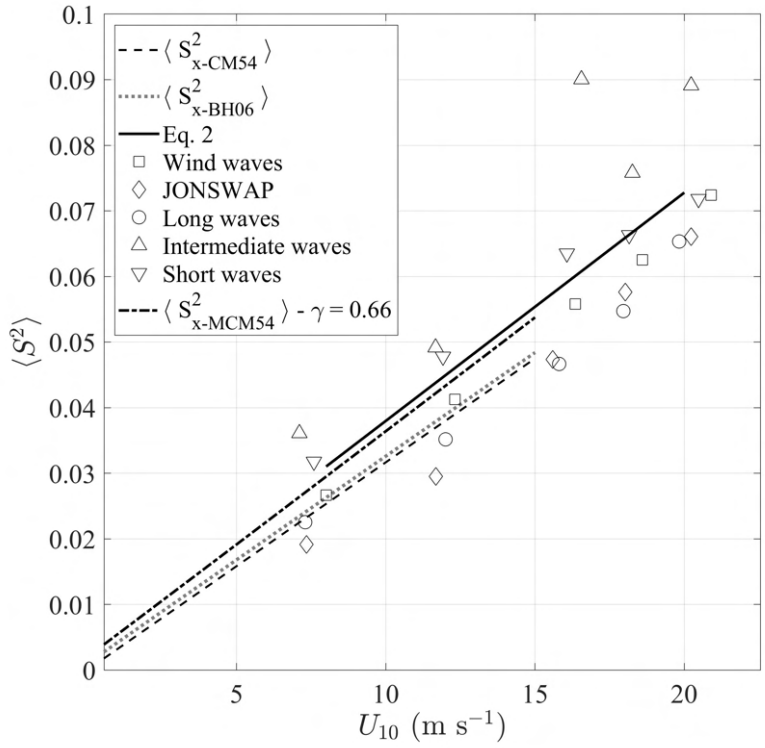

Figure 2. Wave-slope variance as a function of U_{10} wind speed for the upwind laboratory data (black open symbols and black solid line), and the upwind components of CM54 (dashed line) and BH06 (dotted line). MCM54 (dashed-dotted) represents the modified total CM54 wave-slope variance with $\gamma = 0.66$.

Longer swell-type waves can by uncorrelated with the local wind speed. Despite this, the possible modulation of sea spray generation by longer wave components is neglected. Wind-wave-ocean coupled models have been shown to improve the accuracy of weather models in extreme events (Pianezze et al., 2018; Sauvage et al., 2021). Beyond the more generic open ocean studies, the study of sea spray generation extends to a range of environments such as lakes (Harb & Foroutan, 2022) and coastal areas (van Eijk et al., 2011), where wave behaviour is expected to be different. The increasing availability of wind-wave-ocean models promise a greater sensitivity to the many complexities of the marine environment, such as wave-wind interactions by wave-current (Romero et al., 2017; Marechal & de Marez, 2022) and wave-bottom interactions (Anctil & Donelan, 1996; Taylor & Yelland, 2001). In future study, it should be interesting to persue investigation on possible $\langle S_x^2 \rangle$ modulation by different wave types, as is apparent in Fig. 2.

In summary, MATE19 laboratory measurements yield a first order linear relationship between the upwind wave-slope variance $\langle S_x^2 \rangle$ and the horizontal wind speed U_{10} that is comparable to the field. We assume that $\langle S_x^2 \rangle$ is solely wind-driven, and consider Eq. 2 to be applicable in the field. This constitutes a first step by the authors towards the understanding of wave-wind interaction at different scales, including between the laboratory and the field. Several explanations to the comparable field and laboratory relationships are presented, such as possible compensation by higher

laboratory wave-slope densities (Wentz, 1976), the integrated contribution of wave breaking to $\langle S_x^2 \rangle$ in the MATE19, and possibly different wave slope directionality.

3 The SUMOS field campaign

3.1 General Presentation

The SUMOS research cruise, funded by the Centre National d'Etudes Spatiales (CNES), took place in the Bay of Biscay onboard the R/V Atalante over 25 days between the 11th February and the 7th March 2021 (cf. Fig. 3). The campaign was led by the Laboratoire d'Océanographie Physique et Spatiale (LOPS), with the contribution of the Mediterranean Institute of Oceanography (MIO) for aerosol and complementary meteorological measurements. The primary goal of the deployment was to validate and calibrate CFOSAT SWIM and SCAT instruments dedicated to the measurement of surface wave and wind fields. In this contribution, however, we focus on the aerosol and meteorological measurements.

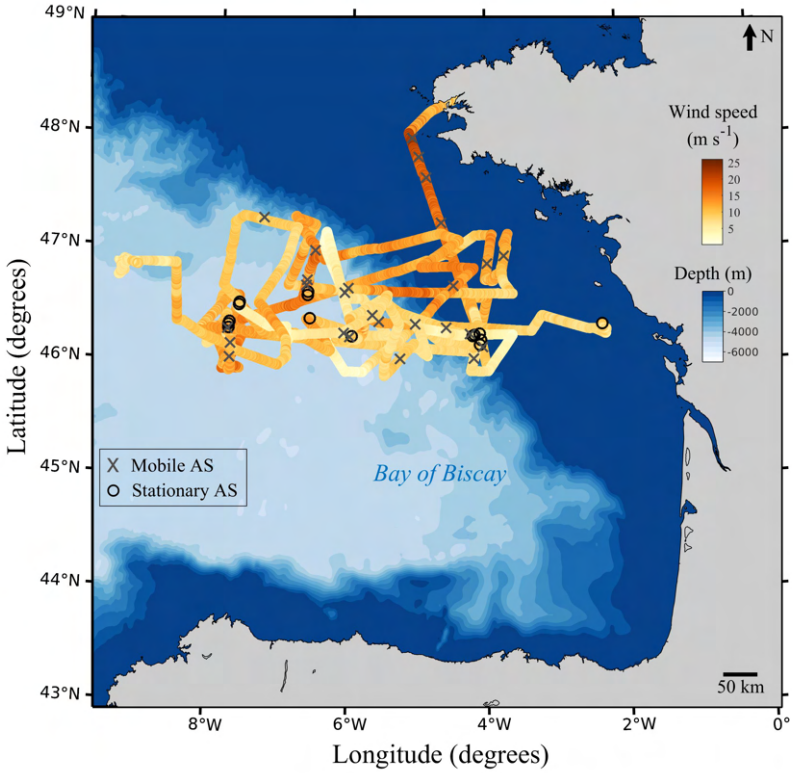

Figure 3. R/V Atalante course during the SUMOS research cruise. The colored dots show the averaged true wind speeds measured at the top of the foremast each minute at each new vessel location. The colored background represents the bathymetry using the ETOPO1 (Amante & Eakins, 2009) product, and shows the extent of the continental plateau at $\approx$ 200m depth or less.

Marine aerosol and meteorological measurements were continuous during the campaign, except for occasional maintenance. Along the vessel's path presented in Fig. 3, a total of 41 aerosol stations (AS) were identified (shown by "$\circ$" and "$\times$" symbols) from the campaign dataset by selecting segments that meet a number of requirements. These are the stationarity of measured variables over the duration of

each station, as well as the sufficiently long time on station to allow good particle count statistics for all measured particle sizes (0.1–47.5µm range) (cf. Sect. 3.2.1). A further requirement is the maximum 45° angle between the CSASP inlet direction (aligned with the ship bow) and the true wind direction is required for aerosol probe sampling to be optimal, and to limit possible flow distortions around the bow (Dupuis et al., 2003; Bourras et al., 2009). The aerosol stations are separated into two categories: 1) stationary aerosol stations (SAS) corresponding to measurements made when the ship was stationary (black "$\circ$" symbol in Fig. 1) with a speed below 3 knots, and 2) mobile aerosol stations (MAS) corresponding to segments during which measurements were acquired whilst the ship was on the move (dark grey "$\times$" symbol in Fig. 1) at speeds above 3 knots, reaching up to 11 knots. This distinction is a precautionary measure relative to the marine aerosol measurements. The apparent wind speed resulting from the combination of true wind speed with ship motions may reach values capable of altering the flow rate in the CSASP probes, despite the isokinetic (flow regulating) nature of the probe inlets. Furthermore, elevated ship speeds would sometimes lead to strong impacts of waves against the bow, capable of ejecting sea water droplets into the air. Some rare and very short peaks in concentrations were noted during the processing of the data, but were not removed as they represented minimal significance relative to the average concentrations.

3.1.1 Instrumentation

The meteorological and aerosol setup is presented in Figure 4. The two-dimensional wind field (u and v horizontal components) is measured at the foremast and the main mast with WindObserver II 1390-PK-006/10M (Gill Instruments Limited, Hampshire, UK) ultrasonic anemometers (Figs. 2c & 2e). The MeteoFrance weather station located in the main mast measures atmospheric variables such as relative humidity, air temperature (HMP35DE sensor - VAISALA, Vantaa, Finland) and water temperature (PT100-type sensor) at 1Hz, approximately 28 meters above the MWL (cf. Fig. 2e).

For the measurement of aerosol concentrations, four classical scattering aerosol spectrometer probes (CSASP) (Particle Metrics Inc., Boulder, Colorado) were positioned at the front of the ship (cf. Figs 2a–b), and split into two sample locations, denoted L1 and L2. The CSASP-200 probes measure concentrations over 31 particle size bins of widths ranging 0.01–1.5 µm radius, whilst the CSASP-100-HV and CSASP-100-HV-ER measure concentrations for a total of 60 particle size bins (rotating over one of four sets of 15 bins every 2 minutes) with bin widths ranging 0.25–1.5 µm radius and 0.5–3 µm radius, respectively. All four probes provided outputs at a frequency of 1 Hz.

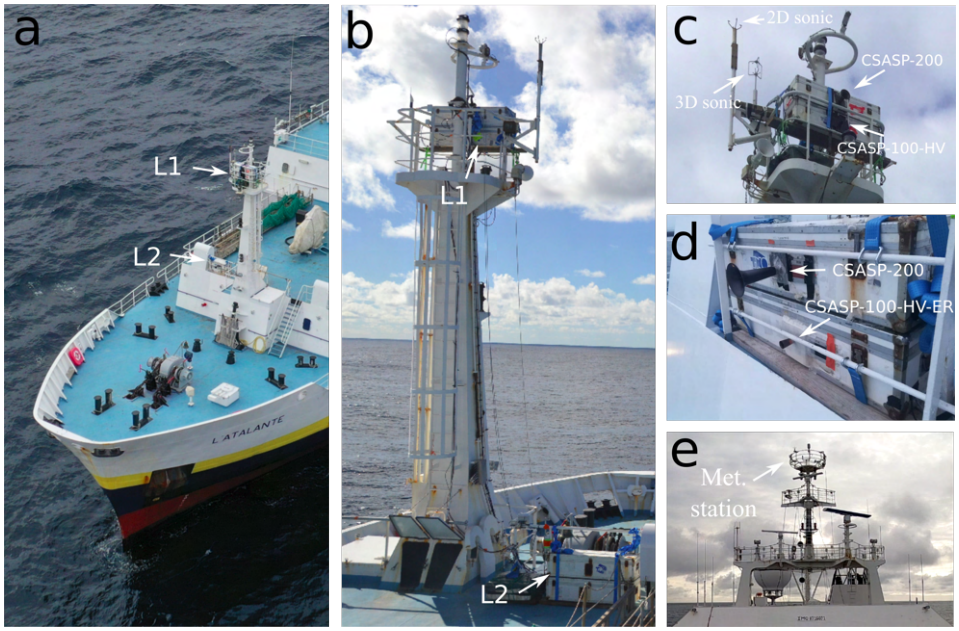

Figure 4. An aerial drone view of the (a) front and (b) back of R/V Atalante's foremast. Front-views are shown of the two CSASP sensor couples in their protective cases at sample locations L1 (c) (courtesy of Emma Bent – LOPS) and L2 (d). (e) Photograph of the main mast and the meteorological station.

A CSASP-200 (0.1–9.25µm radius) and a CSASP-100-HV (0.5–22.75µm radius) were placed high in the foremast (Fig. 2b–c) for the measurements of size-dependent concentrations over the 0.1–22.75µm radius range. This location is referred to as L1. On the basis of waterline measurements made at the beginning and the end of the campaign, the mean height of the foremast platform above the MWL during the campaign is estimated at 15.4 meters. Positioned above one another, and raised approximately 50 cm above the foremast platform to further reduce possible perturbations caused by a nearby ship navigation light, L1 CSASP-100-HV and CSASP-200 inlets were approximately 16 and 16.2 meters above the MWL, respectively. The L1 station is considered the most reliable, as this location is thought to be less impacted by air flow distortion induced by the vessel structure (Dupuis et al., 2003; Bourras et al., 2009), as well as bow splashing. L1 is therefore the main focus of the following study.

At the foot of the foremast, where larger particles are expected to be more frequent, a CSASP-100-HV-ER and a CSASP-200 allow to cover the 0.1–47.5µm radius range. At this second sample location, L2, the CSASP-100-HV-ER and CSASP-200 inlets were respectively located 8.95 and 9.15 meters above the MWL. Though the L2 probes are positioned above the bow, it is likely that the airflow is more perturbed by splash droplets and the ship's structure, especially for smaller particles that have a higher response to turbulence. L2 data is not used in this study.

3.1.2 Environmental conditions

More than 9 days with wind speeds greater than 10 m s^{-1} were recorded at the foremast. These conditions accompanied with wave breaking were favourable for sea spray generation. Spume droplet ejection from breaking wave crests was observed

above the 12 m s^{-1} threshold (E. Monahan et al., 1986; Andreas et al., 2010) and captured on photographs (not shown here). The expedition set out from the port of Brest (France) on February 11^{th} with low atmospheric temperatures nearing zero degrees Celsius, and strong North-Easterly winds exceeding 20 m s^{-1}. Within 24 hours, the vessel reached the study area and was met with warmer atmospheric conditions. Other than during the intial cold spell, air and water temperatures were similar on average, with respective overall average temperatures of ≈11.5°C and 12.0°C. A persistant anticyclone positioned over the European continent prevented Westerly depressions originating off the North-American coast from reaching the study area during most of the campaign duration. This mostly led to Southerly and North-Easterly winds in the study area (cf. Fig. 5b), which regularly resulted in fetch-limited conditions with proximity to Spanish and French coastlines, sometimes accompanied by South-Westerly swell. A hazy layer close to the sea surface was also observed in these high wind conditions, and was most likely associated to sea spray generation.

The timeseries of key meteorological measurements are presented in Fig. 5. The true wind speed and direction at the main mast and foremast were calculated from the vessel course, apparent wind speed and direction. As shown in Fig. 5a, a wide range of conditions were met, with foremast (grey line) and main mast (black line) wind speeds spanning 1–20 m s^{-1}. Gaps in the data correspond to when the aerosol probes were not operating. The air (solid yellow curve) and the water (blue solid curve) temperature are represented in Fig. 5c. As a result of the small average air-sea temperature gradients, weak air-sea heat fluxes and neutral atmospheric conditions are assumed. Relative humidity (RH) was measured continuously during the campaign, though issues with the main sensor resulted in some data gaps towards the end of the campaign. At 28 meters above the MWL, the average RH over the entire campaign was equal to 73%. Following classical humidity profiles at sea, the average RH at the heights of L1 and L2 can be expected to be closer to 80%. Another humidity sensor placed at the foot of the foremast adjacent to L2 became saturated very early and throughout the campaign, most likely as a result of sea spray. This highlights the challenge of performing measurements in high wind speed conditions in which the air near the surface is heavily loaded with sea spray droplets.

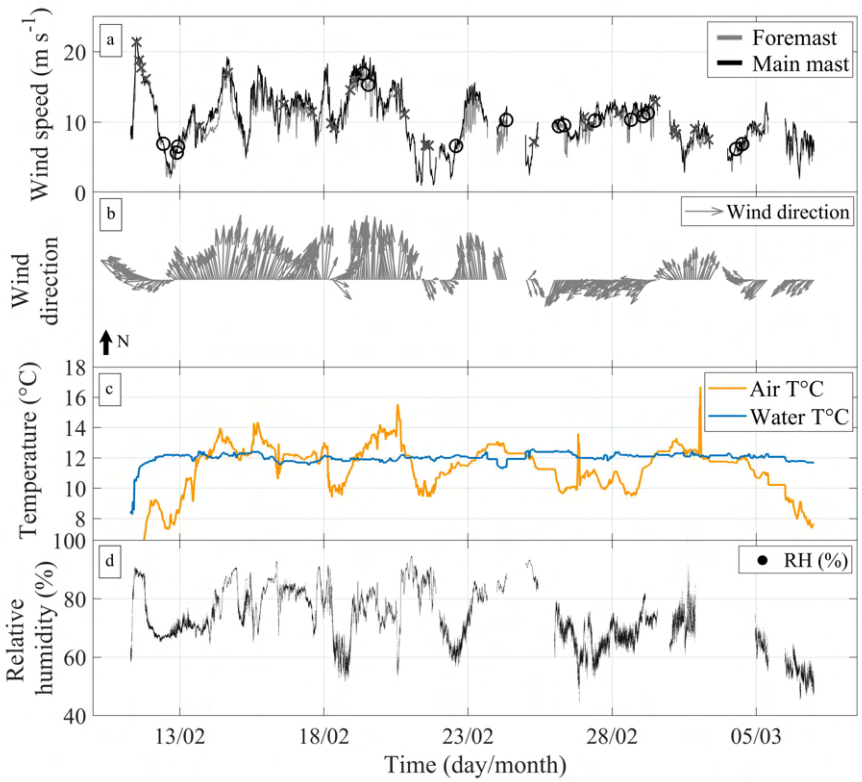

Figure 5. Meteorological data collected onboard R/V Atalante. (a) the timeseries of the true wind speed (m s^{-1}) measured at the main mast (black solid line) and the foremast (grey solid line). "×" and "○" symbols indicate the MAS and SAS stations. (b) the true wind direction represented by grey arrows (up is North), the lengths of which are proportional to the wind speed. (c) shows the air (orange solid line) and water temperature (blue solid line), in degrees Celsius. (d) shows the relative humidity (%).

3.2 Marine Aerosol Measurements

3.2.1 Sampling Correction Methods and Stationarity

Prior to the field campaign, the four CSASP probes were tested in the laboratory. In the absence of wind, all probes were set to measure the same background noise. The L2 probe concentrations were adjusted to the two reference L1 probes, calibrated with latex particles of known sizes prior to the experiment. After correction, L1 and L2 probes perform well against each other, with $R^2 = 0.99$ and $R^2 = 0.96$ respectively. Prior to the SUMOS deployement, the flow speed in the probes was monitored as a function of the incident wind speed. Probe output airflows were measured in the Pytheas Institute tunnel over the entire 0–15 m s^{-1} wind speed range of the facility. Results reveal that the CSASP-100 probes show little sensitivity to the incident wind speed, unlike the CSASP-200 sensors that show a 25% increase in flow speed relative to factory settings at 15 m s^{-1} (cf. Appendix A). It is possible to correct CSASP-200 concentrations as a function of the wind speed measured near the probe inlet, up to the 15 m s^{-1} limit allowed at the LASIF for the elaboration of the correction function. Beyond this limit, the behaviour of the probe is not well known.

The physical variables measured at each sample station (cf. Sect. 3.1.2) must be stationary over the duration of the considered segment, which has to be as long as possible to ensure maximum aerosol count statistics. Here, stationarity pertains to winds and waves, as these two quantities determine sea spray generation and transport. In the present study, station durations range from 40 to 220 minutes, and cover 90 minutes on average. For wind velocities measured at the foremast, stationarity is first verified with normal-like probability density functions (PDFs) obtained at each individual station. Generally, strong symetricity can be observed for sample durations above 15 minutes, all the way up to the maximum station lengths. The stationarity of sea spray concentration measurements is also investigated for each individual particle size bin. For the rarer and larger particles, longer sampling durations sometimes exceeding 1 hours are required, lest the PDF peak be incomplete or truncated. The convergence of sea spray concentration averages was also verified. Following these tests, we set 5 particles per size bin as the lowermost number of droplets that need to be counted over the average station duration. Considering the CSASP probe sample rate of approximately 12 cm^3 s^{-1} and the average station duration, concentrations below 6.15×10^{-5} (cm^{-3} μm^{-1}) are discarded. This led to particles exceeding 20 µm radius not to be considered. Such constraints highlight the significant challenge of measuring spume droplets in the field, and the very limited knowledge we have of them. The authors discuss measurement alternatives later in the article (cf. Sect. 5.2).

3.2.2 Sea Spray Measurement Results

The dependence of sea spray distributions on wind speed during SUMOS is investigated. The 11–12th February peak in wind speed leads to the highest measured concentrations for radii greater than 5µm (cf. timeseries presented in Sect. 4.2.2, Fig. 8c–d), with almost 3300 and 400 hourly counts made by the L1 CSASP-100-HV probe for particles of 10 and 20 µm radius, respectively. The two solid lines shown in Fig. 6a are polynomial functions fit to the averaged sea spray distribution spectra computed from L1 CSASP-100-HV measurements at two stations. At the MAS21 station, U_{10} = 6 m s^{-1} (black solid line and "+" symbols) concentrations rapidly decrease with increasing droplet radius ($r \gtrsim 5\mu m$), as the wind speed is too low for the activation of spume droplet generation. The hump likely represents the jet droplet mode, which is known to be activated for winds above 4 m s^{-1} (Blanchard, 1963; Spiel, 1994). At the MAS02 station, U_{10} = 18 m s^{-1}, concentrations (grey solid line and "$\circ$" symbols) are higher over the entire size range, especially above 10 µm radius, with the contribution of a possible spume droplet mode extending the distribution to the maximum measurable droplet radius of 22.75 µm. Aerosol number concentrations are generally found to be highest for the highest wind speeds, as shown in Fig. 6b for droplets of 4.5 µm radius. The increase in concentration with wind speed seems to tend towards a plateau, similar to that reported for whitecap coverage by (de Leeuw et al., 2011) or the surface drag (Edson et al., 2013), among others.

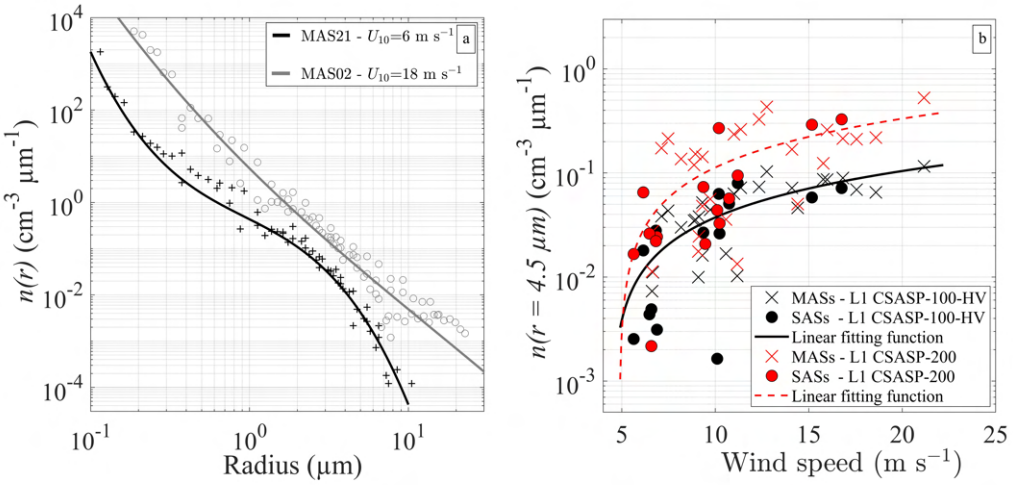

Figure 6. (a) Aerosol distribution spectra showing number concentrations obtained with the L1 CSASP-100-HV as a function of particle radius. Mobile station data are presented with respective U_{10} wind speeds of 6 (grey solid line and circles) and 18 m s^{-1} (black solid line and plus signs). In (b) the L1 CSASP-100-HV (black symbols and line) and CSASP-200 (red symbols and line) number concentrations at 4.5µm radius are shown as a function of the foremast true wind speed. Linear functions fit to the 41 stations show the overall relationships for the individual probes.

As an alternative for the linear fits shown in Fig. 6b, power laws can be used. Power laws have been used to relate ocean surface characteristics to wind speed in a wide range of studies, such as to scale whitecap coverage (e.g. E. C. Monahan and Muircheartaigh (1980); de Leeuw et al. (2011)). They are found to be a better choice to describe the relationship between concentrations and wind speed for particles near or larger than 5 µm. For example, $R^2 = 0.57$ at 5 µm and $R^2 = 0.72$ at 18 µm (not graphically shown here). The weakening of the relationship for smaller droplets, which incidentally tends to become linear (cf. Fig. 6b), illustrates how they may be less related to the local sea spray generation flux. We must also consider that sea state characteristics may not be correlated with the local wind speed. The notable deviations in the relationship between concentrations and wind speed (cf. Fig. 6b) suggest that wind speed alone is not sufficient for the scaling of concentration measurements, and better results may be achieved with sea state information (e.g. Lenain and Melville (2017)).

Following previously evoked questions on the ability for CSASP probes to regulate inlet flow (cf. Sect. 3.2.1), we investigate the effects of ship velocity on the aerosol probes. Across the 41 stations, relative wind speeds at mobile aerosol stations are on average 4 m s^{-1} higher than at stationary aerosol stations. The relationships between concentration and wind speed are compared for the L1 CSASP-100-HV (cf. Fig. 6b, black) and CSASP-200 (cf. Fig. 6b, red) probes, for mobile (MASs, "×" symbols) and stationary (SASs, "•" symbols) stations. The sample volumes of the CSASP-200 probe have been corrected according to the relationship presented in Appendix A. When inspecting the relationships between concentration and wind speed, we note an increasing overestimation by the CSASP-200 relative to the CSASP-100-HV for increasing wind speeds. Furthermore, though not graphically highlighted in Fig. 6b, we find no significant difference between stationary and mobile stations for the CSASP-

100-HV, but concentrations measured by the CSASP-200 were consistently higher at mobile stations, by a factor of 2.5 for true wind speeds lower than 13 m s^{-1}, despite the correction applied to CSASP-200 sample volumes (cf. Sect. 3.2.1 & Appendix A). The discrepancy may still be caused by distortions by the CSASP-200 inlet, and the fact that the airflow used for the sample volume correction was not directly measured in front of the inlet during SUMOS. As a precautionary measure, the data collected by the CSASP-100-HV is used for the remainder of the study.

4 Modeling Sea Spray Transport with the Meso-NH Model

With the urgent need for more accurate sea spray models, the wide range of environmental conditions offered by the SUMOS dataset provides a unique opportunity to validate wind speeds and sea spray modeled by Meso-NH using B21A and B21B SSGFs. Comparison between measurements and numerical simulations is made over 31 SUMOS sample stations encapsulated in the 23 day long Meso-NH simulation period, beginning on 10^{th} February, and ending on 2^{nd} March 2021.

4.1 Configuring the Meso-NH Numerical Model

4.1.1 Meso-NH Model Description

We use version 5.4 of the Meso-NH model (Lac et al., 2018). The model solves the conservation equations of momentum, mass, humidity, scalar variables, as well as the thermodynamic equation derived from the conservation of entropy under the anelastic approximation. The Runge-Kutta methods are applied for the momentum transport, and forward-in-time integration is applied for the rest of the model.

Meso-NH is coupled with the SurfEX module, which allows to simulate the atmosphere-surface exchanges (Masson et al., 2013), and in which our sea spray emission parameterizations are introduced. The module contains the SEAFLUX and the ISBA schemes, which allow to resolve the aerosol, heat, moisture and momentum fluxes at the air-sea interface. Above the surface, the ORILAM aerosol scheme (Tulet et al., 2005, 2010) handles aerosol transport by advection, sedimentation and turbulence, as well as dry and wet deposition (Seinfeld & Pandis, 1997). In the model, three sets of distributions represent the anthropogenic aerosols (which interact with the atmospheric chemistry in Meso-NH) (Tulet et al., 2003), the coarser deserts dusts (Grini et al., 2006), and marine aerosols (Hoarau et al., 2018). In ORILAM, size distributions are defined by lognormal functions (Tulet et al., 2005). A two-moment scheme is used, allowing the total concentration and the median radius of the different lognormally distributed aerosol modes to change. The standard deviation of the lognormal shapes is kept constant through-out the numerical domain. Though not activated in the present study, aerosols in Meso-NH can serve as cloud condensation nuclei (CCN) using the coupling between the ORILAM aerosol scheme and the LIMA 2-moment microphysics scheme (Vié et al., 2016; Hoarau et al., 2018).

4.1.2 Numerical Domain

The model domain is centered on the Bay of Biscay where the SUMOS campaign took place (cf. Fig. 3). The limited westward and northward extent of the model domain (cf. Fig. 10, Sect. 4.2.3) relative to the trajectory of the vessel is adapted to the dominant easterly and southerly winds observed during the campaign, thus limiting possible effects induced by the western model boundary on simulated concentrations. The model is forced by the ECMWF model every three hours. At each interval, predictive modeling allows hourly model outputs. Along the horizontal axis, our North-East Atlantic study area is represented by a domain composed of 300×300 cells. The grid is horizontally regular, with a 2 km resolution. Along the vertical axis, the

atmosphere is composed of 48 layers, ranging from the MWL to 24 km altitude, with an irregular spacing ranging from 5 meters near the surface, to 4000 meters at the top of the domain. An odd-order WENO advection scheme is employed. Considering the 2 km horizontal resolution, numerical stability is ensured by setting the model timestep close to 40 seconds.

4.1.3 Model Sea Spray Parameterization

The choice of sea spray functions parameterized in Meso-NH and presented in this study resides on a prior investigation by Bruch (2022) using the MACMod model (Tedeschi & Piazzola, 2011). These preliminary results indicate that the wind and wave-forced OVA14, B21A, and B21B SSGFs perform well when compared with concentrations measured in the field during the 2008 Mediterranean MIRAMER campaign. OVA14 (Ovadnevaite et al., 2014) is a wind and wave forced SSGF that is adapted for smaller aerosols, i.e., the size range 0.015 – 3 µm (cf. Table 1). The combination of OVA14 with either B21A or B21B ensures that the whole SUMOS size range is respresented. These source functions, presented in Table 1, are selected for the present study numerical simulations.

Table 1. SSGFs parameterized in Meso-NH for the present study.

Parameterization	Size Range (µm)	Scaling Parameter	U_{10} (m s $^{-1}$)
OVA14	0.015–3 (r_D)	$u_* H_s / \nu_w$	3–18
B21A	3–35 (r_{80})	$\langle S_x^2 \rangle$	12–20
B21B	3–35 (r_{80})	$P_S = R_B \langle S_x^2 \rangle \frac{c_p}{u_*}^{-1}$	12–20

Several modifications are necessary before introducing the SSGFs in the Meso-NH model. The B21A and B21B SSGFs need to be adapted (cf. Appendix B) because the model transports moments of the aerosol size distribution with lognormal functions (Seinfeld & Pandis, 1997). Furthermore, the impact of air temperature on sea spray generation is neglected by fixing the air kinematic viscosity to its value at 25°C. This corresponds to the conditions for which B21B was developed on the basis of the MATE19 data. For ambient air temperature of 10°C or lower, it is estimated that changes in air kinematic viscosity could induce a 5% change in the scaling parameter P_S (cf. Table 1). The significant wave height required to force OVA14 (cf. Table 1) was provided by the 0.1 degree resolution ocean-wave WAM model (ECMWF-IFS), based on the work by Komen et al. (1996). Though no validation of the WAM model is performed in this study, this same model was used by Ovadnevaite et al. (2014) for the formulation of OVA14.

Meso-NH also requires speficiation of the droplet density. When using B21A and B21B, the density of the saline sea spray droplets is set to 1172 kg m^{-3}, which corresponds to droplets that have reached their equilibrium radius at 80% ambient humidity. As discussed in Sect. 3.1.2., this approximately corresponds to the average

humidity at the height of the aerosol probes. Not considering these evaporation effects would result in setting the droplet density to 1027 kg m^{-3}, i.e. the droplet density of a freshly produced saline droplet at the surface. Test runs demonstrated that this would lead to 17–19% higher droplet concentrations 15 meters above the MWL, compared to simulations run assuming evaporation effects and an ambient 80% relative humidity. For OVA14, we set the particle density to 2200 kg m^{-3}, corresponding to dry salt particles.

4.2 Meso-NH Modeling Results

4.2.1 Modeling Wind Speed

Meso-NH wind speeds and concentrations predicted 15 meters above the MWL are compared with SUMOS measurements made at a similar height (cf. Sect. 3). A nearest neighbour method is used to find the Meso-NH grid point closest in space and time to the average location of the R/V Atalante during each station. For graphical reasons (cf. Fig. 7–8), the model data nearest to the last known vessel location is used when no match to an existing SUMOS station is found. The comparison is shown in Fig. 7 as a timeseries (Fig. 7a) and as a regression plot (Fig. 7b). The model successfully reproduces the wind speed variations, with R^2 =0.93, as shown by Fig. 7a–b. Over the study period, mean observed and modeled U_{15} wind speeds are 11.61 and 10.6 m s^{-1}, respectively. The model underestimates the wind speed by $\approx 9\%$ relative to observations, with a root mean square error ($RMSE$) of 0.98. Upon close inspection of Fig. 7b, Meso-NH progressively underestimates the experimental observations with increasing wind speed. This can also be observed in Fig. 7a where the model does not successully reproduce the peak of 21.4 m s^{-1} measured on 11–12$^{\text{th}}$ February. The second highest 19–20$^{\text{th}}$ February peak, with observed wind speeds reaching 16.9 m s^{-1}, is very well represented. Overall, the satisfactory model performance for wind speed estimates provides the right conditions to validate the presently wind-forced B21A and B21B SSGFs.

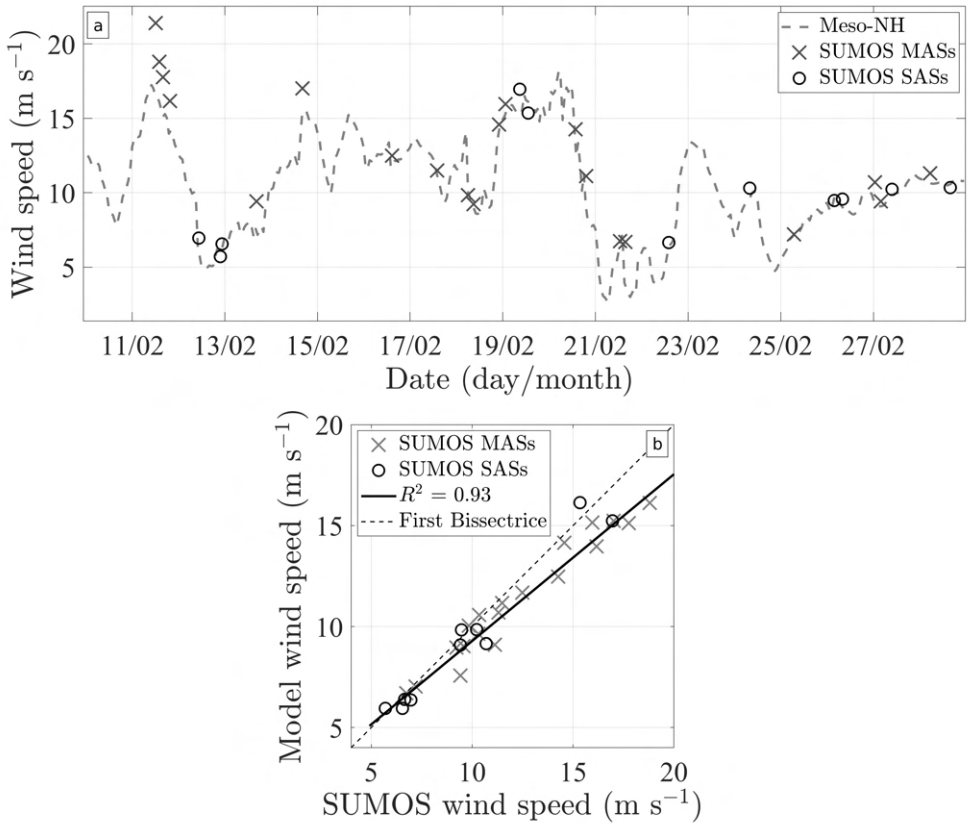

Figure 7. (a) timeseries of SUMOS foremast wind speed measurements at mobile ("×" symbols) and stationary ("○" symbols) aerosol stations, and Meso-NH modeled wind speeds. (b) Regression plot comparing measured (horizontal axis) and modeled (vertical axis) wind speeds at the various stations, and the corresponding R^2 value.

4.2.2 Modeling Sea Spray Concentrations

In this section we compare the modeled and measured aerosol number concentrations. While this has been done for a large number of radii over the measured size spectrum, this section focuses on droplets of 2, 5, 10 and 20 µm radius. As done for wind speed in Sect. 4.2.1, concentrations simulated 15 meters above the MWL are compared with the foremast measurements. The corresponding statistics gathered from the 31 stations are presented in Table 2, i.e. the deviation factor, defined as the ratio of the mean measured $\bar{n}_{obs}$ and modeled $\bar{n}_{mod}$ concentrations. The table also shows model and measurement standard deviations STD_{mod} and STD_{obs}, root mean square errors $RMSE$, and coefficients of determination R^2, are also shown. Figure 8 presents modeled number concentrations obtained with B21B (solid orange line), B21A (solid blue line), and OVA14 (solid black line) SSGFs, alongside SUMOS concentration measurements ("○" and "×" symbols) for four radii, i.e. 2 (Fig. 8a), 5 (Fig. 8b), 10 (Fig. 8c), and 20 µm (Fig. 8d). The number of experimental datapoints decreases for larger particle sizes as a result of the threshold that was imposed for statistically reliable sampling (cf. Sect. 3.2.1.). As previously determined in Sect. 3.2.1, measured concentrations lower than 6.15×10^{-5} are discarded (cf. Fig. 8d). OVA14 performance is not shown for particles greater than 2 µm radius, considering the 3 µm upper validity limit of the SSGF (cf. Table 1). We note that Fig. 8a shows results for

the B21A and B21B SSGFs, although the radius of 2 µm is slightly below their lower validity limit.

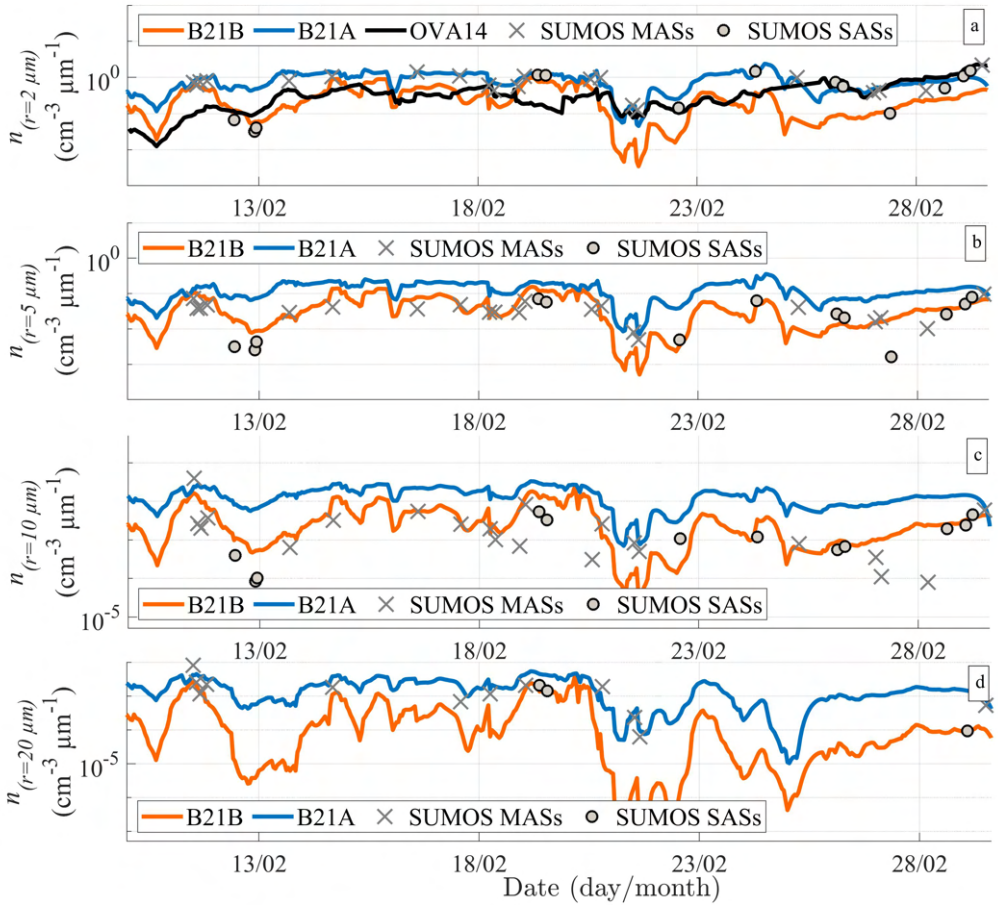

Figure 8. Modeled and observed sea spray concentrations for selected radii (a) 2 µm, (b) 5 µm, (c) 10 µm, and 20 µm. Field observations, namely SASs and MASs, are respectively represented by "∘" and "×" symbols. Simulations using B21A (solid blue line), B21B (solid orangle line) and OVA14 (solid black line) are also represented.

We first compare 2 µm radius number concentrations obtained using the three SSGFs. The OVA14 SSGF yields modest results compared with B21 SSGFs, with concentrations 2.12 times lower than measured in the field, and very low R^2 values of 0.035 (cf. Table 2). By comparing Figs. 7 & 8a, it becomes clear that OVA14 performance is best at low to moderate wind speeds, as is the case after the 25$^{\text{th}}$ February (cf. Figs 7a,8a). At higher wind speeds, the deviation factor can reach values as high as 7. In contrast, the model overestimates the measured aerosol concentrations for smaller radii, e.g., for particles of 0.1 µm (the smallest radii measured by our probes on the R/V Atalante) OVA14 yields deviation factors reaching 4 orders of magnitude. These large discrepancies may point to the absence of efficient deposition mechanisms in Meso-NH for very small particles, which will be investigated in the future.

We now turn our attention to the differences between B21A and B21B. For all radii depicted in Fig. 8, the B21B SSGF demonstrates a particularly good sensitivity to the different wind speed conditions by better reproducing concentrations in higher (e.g. 11–12$^{\text{th}}$ February) and lower wind conditions (e.g. 13$^{\text{th}}$ February) compared

with B21A. This is evidenced by the better statistics (R^2, $RMSE$ and STD), and deviation factors that are closer to 1. Over the 3–20 µm radius range, the deviation factor $\frac{n_{obs}}{n_{mod}}$ varies from 0.36 at 3.5 µm, to 1.1 at 20 µm, with an overall average of 0.7. In terms of concentrations, this corresponds to an overestimation by a factor of 1.5, which we consider a good result in view of typical deviations reported in literature (Chen et al., 2016; Saliba et al., 2019). In contrast, the B21A SSGF generally overestimates concentrations at low to moderate wind speeds, with highest deviations from measurements on the 13$^{\text{th}}$ February, reaching 1 and 2 orders of magnitude at 5 and 10 µm, respectively (cf. Figs. 8 b–c). At high wind speeds, B21A seems to perform well, including over the lower spume droplet range (15–20 µm). The results corroborate the conclusions by Bruch et al. (2021) who found in the MATE19 laboratory experiment that B21B is sensitive to a wide range of conditions, whereas B21A seems adapted to the spume droplet range at high wind speeds.

Table 2. Measurement and model comparative number concentration (cm^{-3} µm^{-1}) statistics for B21A, B21B and OVA14 SSGFs at the 31 stations shared between SUMOS measurements and Meso-NH simulations. Statistical measures include model standard devation STD_{mod}, the $\frac{\bar{n}_{obs}}{\bar{n}_{mod}}$ deviation factor, the coefficient of determination R^2 and the root mean square error $RMSE$ obtained relative to field observations. The standard deviation values of measured sea spray concentrations, STD_{obs}, are also shown. Results are presented for sea spray particles of radii 2, 5, 10 and 20 µm.

	2 µm			5 µm		10 µm		20 µm	
	B21A	B21B	OVA14	B21A	B21B	B21A	B21B	B21A	B21B
$\frac{\bar{n}_{obs}}{\bar{n}_{mod}}$	0.65	1.67	2.12	0.235	0.62	0.21	0.69	0.46	1.1
R^2	0.65	0.47	0.035	0.34	0.60	0.24	0.47	0.16	0.42
$RMSE$	0.18	0.22	0.54	0.02	0.015	5.2 $\times 10^{-3}$	4.3 $\times 10^{-3}$	1.7 $\times 10^{-3}$	1.4 $\times 10^{-3}$
STD	0.45	0.27	0.37	0.07	0.042	8.5 $\times 10^{-3}$	5 $\times 10^{-3}$	1.6 $\times 10^{-3}$	1.6 $\times 10^{-3}$
STD_{obs}	0.33			0.024		5.2×10^{-3}		1.6×10^{-3}	

Although the comparison height of 15 meters above MWL is relatively close to the surface, we can already see some impact of radius-dependent transport. The (experimental and numerical) concentrations of larger (10 or 15 µm) particles scale quite well with wind speed, indicating that a stronger local production is immediately reflected in concentrations at 15 meters. On the contrary, the concentration of 2 µm droplets is less clearly related to the local wind speed, as shown by the example of higher concentrations observed over the 14–18$^{\text{th}}$ February period, marked by lower wind speeds. This corroborates the stronger relationship between the local wind speed and sea spray concentrations for the larger droplets, previously reported from measurements (cf. Sect. 3.2.2).

4.2.3 Sea Spray Transport Beyond the Mixing Layer and Over Land

As discussed in the introduction of this manuscript, significant uncertainties exist on the distribution and concentrations of sea spray in the Earth's atmosphere, and thus, their contribution to weather and climate. The Meso-NH B21B configuration provides us with a tool to study sea spray transport, and to investigate its presence in and above the atmospheric boundary layer, both over marine and land surfaces. In the following we will consider two events. The first event took place on 10th February, when an East-bound North Atlantic depression with strong winds up to 20 m s^{-1} was located in the South of the Bay of Biscay. This event resulted in strong updrafts allowing for efficient vertical transport of sea spray. The second event took place on 16th February when a persistent westerly flow with winds around 15 m s^{-1} was present over the Bay of Biscay, resulting in a rather classical boundary layer with long fetch lengths and neutral conditions, favorable for the transport of sea spray over France. The two events are presented in Figs. 9 and 10, where the left and right panels represent the first and second event, respectively. Figure 9 shows Meso-NH simulations of the horizontal wind field (top panels) and concentrations of 10 µm sea spray droplets (bottom panels). Fig. 10 shows vertical transects extracted along T1 and T2 (cf. Fig.9), allowing to observe the vertical distribution of 10 µm droplet concentrations (top panels), as well as the turbulent kinetic energy TKE (bottom panels). The horizontal axis denotes the distance from the left boundary of the numerical domain (cf. Fig.9).

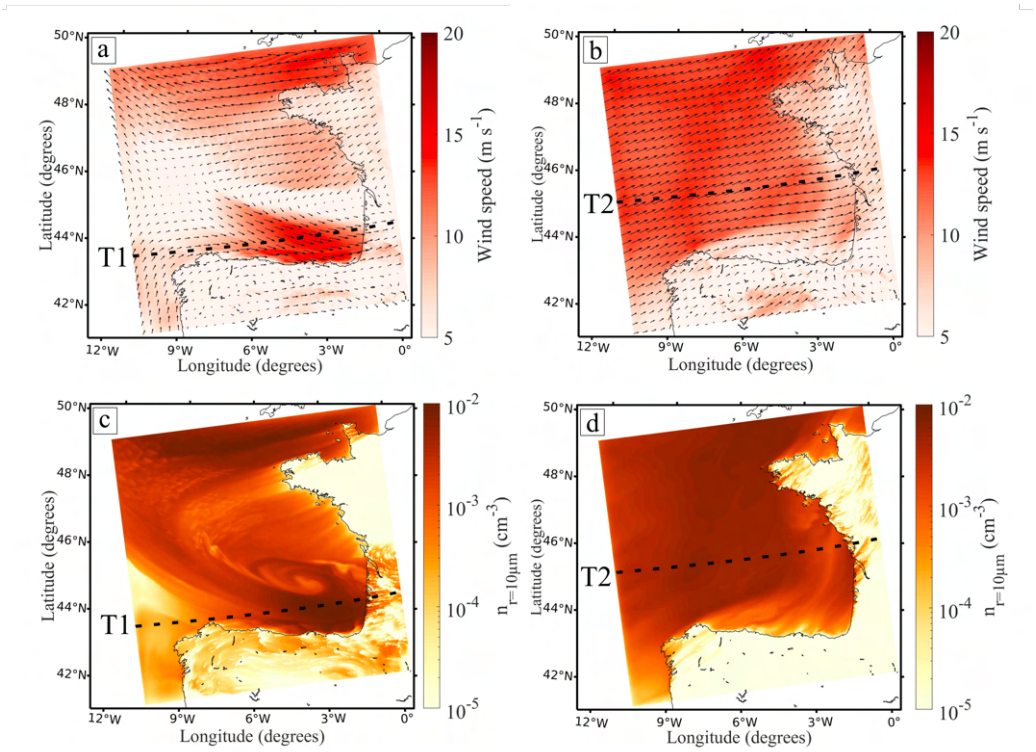

Figure 9. Meso-NH outputs using the B21B SSGF on (a,c) 10th February 2021 at 12AM UTC, (b,d) 16th February 2021 at 11AM UTC, at 15 meters elevation. Top panels show wind speed and direction. Bottom panels show concentrations for droplets of 10 µm radius.

For the first event, Fig. 9 shows a snapshot taken on 10th February at 12 UTC when wind speeds were decreasing as the low pressure system had started to subside and made landfall. Fig. 10 shows the concentration data extracted along T1

for that same timestamp, along with a contour line (solid line) that indicates the 10^{-3} cm^{-3} µm^{-1} threshold, which we have determined as the threshold above which concentrations are significant. To provide an indication of the temporal evolution of concentrations, dotted and dashed contour lines in Fig. 10a represent snapshots on 10$^{\text{th}}$ at 9 UTC and 24 UTC, respectively. For the second event, both Figs. 9 and 10 present a snapshot for 16$^{\text{th}}$ February at 11 UTC, when the steady westerly winds had created a well-developed marine atmospheric boundary layer (MABL).

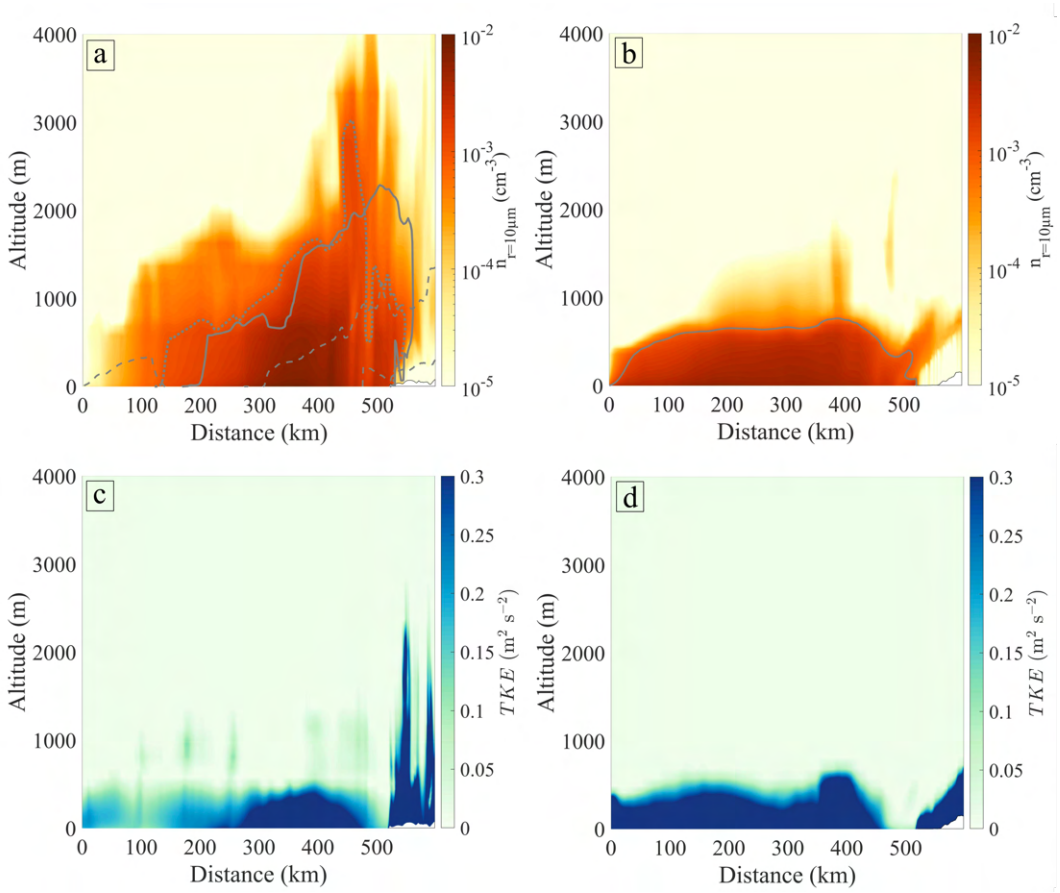

Figure 10. Vertical cross-sections of sea spray 10 µm concentrations and TKE along T1 on 10$^{\text{th}}$ February at 12 UTC (a,c), and along T2 on 16$^{\text{th}}$ February at 11 UTC. Grey contours show the extent of the 10^{-3} cm^{-3} µm^{-1} concentration threshold at Time+0 hours (solid line) (a,b). In panel (a) contours are added at 9 UTC (dotted line) and 24 UTC (dashed line) UTC.

On 16$^{\text{th}}$ February, fetch lengths in the numerical domain reached approximately 400 km, allowing sea spray droplets to reach an equilibrium height in the whereabouts of the 350 km mark along T2 (cf. Fig. 10b). At the 350 km mark, the 10^{-3} cm^{-3} µm^{-1} number concentration threshold for droplets of radius 3.5, 10, 15 and 20 µm reach heights above the MWL of 950, 684, 40 and 10 meters, respectively. This can be verified for 10 µm droplets in Fig. 10b. The height of the mixing layer, usually spanning from several meters above the MWL to the top of the MABL, is highly dependent on the TKE (cf. Fig. 10d) as the latter is associated with the vertical aerosol transport flux through turbulent diffusion (e.g. Fairall and Davidson (1986)). At this same 350 km mark, the TKE transect shows values of 0.5 m^2 s^{-2} at 500 meters altitude, and a sharp decrease around 700 meters. This sharp decrease marks the top of the MABL, above which we observe near-constant TKE values and near-homogenous

concentrations as a function of height as we enter the mixed layer. Between the 400 km and 500 km mark, lower wind speeds and smaller values of TKE near the coastline result in a relatively low vertical sea spray transport flux and dominant gravitational settling with a decrease in the vertical extent of sea spray concentrations, and therefore of the MABL (cf. Fig. 10b).

For both events, marine airmasses are transported towards the Western coast of France. At the intersection between air and sea, such as between the 500 and 600 km mark in both T1 and T2 (cf. Figs. 10c–d), high TKE values are observed as the surface topography, and inherintly the surface roughness, are radically changed. This signals the formation of a turbulent coastal internal boundary layer (herein CIBL), which is known to be generated as a result of rugosity and possible thermal effects over land, as shown by Augustin et al. (2020) for the transport of pollutants during a sea breeze. The marine airmass, rich in sea spray, experiences an updraft as required by continuity (Bradley, 1968; Garratt, 1990) and are lifted above the CIBL, and eventually the land boundary layer, by approximately 200 meters in Fig. 10a (e.g. dashed contour lines) and Fig. 10b (color scale). This rise of the sea spray plume can explain the low concentrations observed in this internal sublayer. Another possible contribution to this is the high turbulent dispersion of the portion of the aerosols that do enter the CIBL, with high local TKE (cf. Figs. 10c–d). As the air mass moves further inland and away from the sea spray production zone, the concentration gradient of the aerosols becomes negative as gravitational settling becomes more prominent. As expected, the larger particles are rapidly deposited through gravitational settling. The smaller particles that experience less gravitational settling become a more and more dominant fraction of the total atmospheric aerosol population over the continent. Consequently, the smaller 3.5 µm particles are still present in sizeable concentrations at the very eastern part of the numerical domain (10^{-2} to 10^{-3} cm^{-3} µm^{-1} as compared to the lower $5{\times}10^{-5}$ to $5{\times}10^{-4}$ cm^{-3} µm^{-1} concentration range for 10 µm droplets, cf. Fig. 10d).

Figures 9 and 10 reveal additional responses of the sea spray concentrations to environmental conditions. Whereas the previous discussion focused on aerosol dispersion in the MABL and their horizontal transport over sea and land, we will now discuss vertical transport to altitudes well above the MABL. To this end, we will return to the 1st case (10th February 12AM (UTC), cf. Figs. 9a,c and 10a,c). As the depression moves across the Bay of Biscay, filament-like patches of higher and lower concentration air masses alternate, reminiscent of gyre and eddy surface signatures (cf. Fig. 9a). Using our Meso-NH simulations, this frontal depression characterized with cold air and warmer sea surface temperature (cf. Fig. 5c) is predicted to drive convection and significant cloud formation in the air column over the 400 km mark, with modeled cloud cover spanning 0.5–4.5 km altitude. Amid convective cumulonimbus formation occuring on 10th around 8 UTC (not shown here), relatively high turbulence is observed in the air column with high TKE values of approximately 0.5 m^2 s^{-2} at 2 km altitude, which do not significantly defer from the 0.6 m^2 s^{-2} value 500 meters above the MWL. As evidenced by the vertical cross-section shown in Fig. 10a, numerical simulations reveal the remarkable vertical extent of sea spray plumes reaching beyond the MABL and up to 3300 meters altitude in the case of 10 µm particles in the air column over the 450 km mark. For the same event, 3.5 µm and 15 µm droplets show modeled concentrations above the threshold value up to 5000 and 400 meters altitude, respectively (not shown here). The convective transport simulated by Meso-NH during the first case (10th February) therefore results in a much higher vertical extent of sea spray compared with the second case (16th February). Though sea spray do not intervene in cloud physics in the present study simulations, our results show that droplets can be transported to altitudes where they can contribute to cloud processes, over the film and jet range especially. The larger spume droplets are less efficiently transported vertically, which is confirmed by the lesser vertical extent of these droplets in both events

presented here. Analagous to the second case, the sea spray transported by the wind reaches land, and an IBL is formed. Sea spray plume reach higher altitudes of up to 1.2 km over land on 11 th February at 0 UTC (UTC, cf. Fig. 10a, dashed contourline). This reserve of sea spray ejected into the higher layers of the atmosphere progressively deposits to the surface, as the wind speed decreases and the IBL collapses in the early hours of the 11th February. This sea spray deposition over land as the IBL subsides corroborates the known relationship between size-dependent dry deposition and the predominance of laminar or turbulent regimes in and around a surface boundary layer (e.g. W. Slinn et al. (1978); Carruthers and Choularton (1986); Fairall and Davidson (1986)).

The three-dimensional study of sea spray dynamics in Meso-NH show that the size range represented by the laboratory SSGFs is transportable in the atmosphere. Sea spray is present over the continental with significant concentrations reaching 100 km inland all the way to the model's East boundary. In cases of strong sea spray generation during a frontal convective event, sea spray droplets are ejected more than 2500 m above the sea level. Sea spray over the smaller film and jet range are therefore available to contribute to a range of atmospheric processes such as cloud microphysics and radiative forcing. Spume droplets are less efficiently transported over the study size range, but successfully transit through the evaporation layer, thus contributing to air-sea fluxes such as that of latent and sensible heat.

5 Discussion

5.1 On Using Laboratory $\langle S_x^2 \rangle$ in the Field

The necessity to consider the integral part of the gravity wave spectrum for a complete multiscale representation of the free surface geometry motivated the study of laboratory $\langle S_x^2 \rangle$ by Bruch et al. (2021). In the present study, whilst the multiscale $\langle S_x^2 \rangle$ drives sea spray generation, the assumed unique dependence on wind speed (cf. Sect. 2) reduces SSGF sensitivity to environmental caracteristics such as sea state. The influence of wave type is shown from MATE19 laboratory data (cf. Fig. 2, Sect. 2), but further study is required to understand the effects of non-linear wave-wave interactions on wave-slope variance, as the different wave scales between the laboratory and the field may change how they interact. As suggested by Plant (1982) and Donelan (2001), wave-wave non-linear interactions may modulate the contribution of different wave components to $\langle S_{x,y}^2 \rangle$. Furthermore, the similar relationship between laboratory (Bruch et al., 2021), airborne (Cox & Munk, 1954) and satellite-derived formulations (Bréon & Henriot, 2006) raises a number of questions on $\langle S_{x,y}^2 \rangle$ dependence on wave state, wave spectrum density (Wentz, 1976) and directionality (Hauser et al., 2008; Romero & Lubana, 2022). As a possible answer, we suggest developing an analytical approach to scaling according to a wave-scale-dependent reference height, in a vein similar to a wave height-dependent effective height described by Iida et al. (1992) or Chalikov and Rainchik (2011) among others. Future improvement to this work should include the dependence of the multiscale $\langle S_x^2 \rangle$ on both the longer swell-type wave components and near-surface wind characteristics in the field.

5.2 On Sea Spray Sampling

The aerosol measurements during the SUMOS campaign suffered from poor count statistics for particles larger than 20 µm, despite average sampling durations of 90 minutes. Considering that spume droplets are not efficiently transported in the air flow, their concentration is most abundant close to the production zone and at heights below, say, 12 meters above the MWL (Sect. 4.2.3). This may explain the low count statistics, because the probes are generally located at some distance from the source, e.g., on the coast (e.g. (Smith et al., 1993; Piazzola et al., 2009)), at deck height on a

vessel (Laussac et al., 2018), or airborne (Fairall et al., 2014; Lenain & Melville, 2017). The difficulty to sample large enough numbers of large spume droplets highlights the need to find metrological alternatives. Recent studies have also proposed the use of remote sensing techniques (Xu et al., 2021). Another promising alternative is the deployment of instruments onboard autonomous surface vehicles (e.g. Grare et al. (2021)).

Regardless of the preferred metrology, all instrumentation should be thoroughly verified to avoid issues such as reduced sampling efficiency (cf. Sect. 3.1.1 and Fig. 6b). It is here that wave-wind laboratories offer an promising alternative, because conditions are more controlled and instrument artifacts can be more easily detected than in the field. However, attempts have been rare to compare field and laboratory aerosol concentrations (Iida et al., 1992) and generation fluxes (Nilsson et al., 2021). To our knowledge, this has never been achieved over the jet and spume droplet dominance ranges, as a result of the absence of a reliable experimental approach for the estimation of the generation flux in the field.

5.3 Towards a Complete Marine Aerosol Spectrum in Meso-NH

During the SUMOS campaign, we assume that all measured aerosols are of marine origin. However, a variety of aerosol types can coexist, in coastal zones especially. In future studies, more realistic atmospheres should include other species than sea spray. This partly motivated the use of the OVA14 SSGF (Ovadnevaite et al., 2014) in Meso-NH, to extend the study to submicronic marine aerosols. Unfortunately, this led to an overestimate of the concentrations of smaller particles by Meso-NH relative to those measured during the SUMOS campaign. We list some reasons that may explain this. This discrepancy may point to the lack of efficient aerosol sinks in the model, e.g., scavenging by rain (W. G. N. Slinn, 1983) and dry deposition. Alternatively, OVA14 may be overoptimistic about the actual production, or the measured concentrations may be underestimated because of issues with the CSASP-200 probe. It is would be worthwhile to run Meso-NH with other SSGFs than OVA14, but this could not be achieved in the present study due to funding constraints.

Effects such as evaporation, and the contribution of sea state, are neglected in the simulations. Future efforts should include such effects, as droplets are expected to encounter strong humidity and temperature gradients as they transit in the MABL and beyond. Though previously led by computationally intensive Lagrangian modelling efforts (Veron, 2015), advances have led to the proposal of Eulerian models for the study of droplet-driven evaporation (Veron & Mieussens, 2020) and momentum transport (Rastigejev & Suslov, 2022).

6 Conclusion

Often overlooked, some authors have highlighted the importance of considering the contribution of the shorter wave components and geometric surface complexity to wind and wave-driven air-sea interaction (Plant, 1982; Jähne & Riemer, 1990; Bock et al., 1999; Kudryavtsev et al., 1999; Munk, 2009). Edson et al. (2013) confirmed this by showing that peak wave parameters cannot reveal all the intricacies of the air-sea momentum flux. However, the wave-slope variance offers a multiscale description of the sea surface, and was used in previous work (Bruch et al., 2021) to scale the laboratory sea spray generation flux. Considering that the nondimensional slope of roughness elements such as waves drives airflow separation and wave breaking (e.g. Stokes (1880)), the laboratory SSGFs proposed by Bruch et al. (2021) encapsulate the key mechanisms that drive sea spray generation.

As part of our bottom-up approach, the real world validity of laboratory SSGFs is tested in the present study using the Meso-NH atmospheric model (cf. Sect. 4). Since wave-slope variance is not available as a forcing parameter in this environment, the laboratory relation between $\langle S_x^2 \rangle$ and U_{10} (Eq. 2, Sect. 2.1) is used for evaluating the sea spray generation flux. This is equivalent to the previously proposed relations between $\langle S_x^2 \rangle$ and U_{10} in the field (Cox & Munk, 1954; Bréon & Henriot, 2006), assuming a negligible modulation by the longer swell-type wave components. The relation given by Eq. 2 is observed and employed for the parameterization of the SSGFs in the model.

The numerical wind speed (Sect. 4.2.1) and sea spray concentrations (Sect. 4.2.2) are validated over a wide range of environmental conditions using experimental data acquired during the North-Atlantic SUMOS campaign. Meso-NH succeeds in predicting wind speed over the study period when compared with SUMOS measurements (with $R^2 = 0.93$) (cf. Sect. 4.2.1, Fig. 7), which implies that the model provides the correct input parameters to the sea spray generation functions B21A and B21B. The numerical concentrations correspond best to the observations when using the B21B SSGF, which also offers the highest sensitivity to the wide range of environmental conditions. This corroborates with previous results by Bruch et al. (2021) when testing B21A and B21B in a laboratory environment. Overall, the difference between the concentrations predicted with B21B and B21A and those measured in the field was less than the order of magnitude commonly reported in the literature (Chen et al., 2016; Saliba et al., 2019), which is thought to reflect uncertainties in previously reported SSGFs (Andreas, 1998; de Leeuw et al., 2011; Veron, 2015). Our results thus show that the Meso-NH B21B model configuration can be a valuable tool for future studies of sea spray dynamics in the atmosphere. Considering the scarcity of sea spray measurements in the field, the SUMOS campaign offers a very rare and valuable dataset, that may help constrain weather and climate models (Boucher et al., 2013; Regayre et al., 2020).

A preliminary study towards sea spray transport was made with the Meso-NH B21B model configuration. As discussed in Sect. 4.2.3., the model predicted that significant sea spray concentrations could be found in the atmosphere over the continent, up to 100 km inland. As maritime air flows over land, high TKE values are observed as the surface roughness is radically changed, and a new and turbulent internal sublayer is generated. The marine airmasses, rich in sea spray, are found to be lifted above this sublayer. Low concentrations in the internal sublayer are explained by two effects: 1) the rise in the sea spray plume, and 2) the high turbulent dispersion of aerosols in the newly formed coastal boundary layer, and the land boundary layers further downwind. During another event, it was found that under convective conditions sea spray droplets can rise to more than 2500 m above the sea surface. This highlighted the importance of atmosphere stability in vertical transport phenomena. Furthermore, the transport of droplets is shown to be strongly dependent on their radius. When sea spray droplets over the film and jet droplet size range are transported so far away from their production zone, they can contribute to a range of processes, such as cloud physics (e.g. Hoarau et al. (2018); Liu et al. (2022)), radiative forcing (e.g. Jacobson (2001); Regayre et al. (2020)) and interaction with atmospheric pollutants. The latter process may impact air quality in coastal areas (Johansson et al., 2019; Piazzola et al., 2021) which are often densely populated. The larger spume droplets are less efficiently transported, and are found closer to their source. The present study shows that the smaller spume droplets are capable of contributing to air-sea heat fluxes by reaching the evaporation layer. Though not studied here, the larger spume droplets most likely remain within the first meters above their emission height.

Acknowledgments

We acknowledge CNRS-CNES for funding the SUMOS research cruise. We also wish to thank the Service Informatique Pytheas (SIP) for their support and the availability of the OSU-Pytheas super computer necessary for the Meso-NH numerical simulations, as well as Quentin Rodier at the Centre National de Recherches Météorologiques (CNRM). We are grateful for the sponsorship by the Agence Innovation Défense (AID-DGA) under contract 2018-60-0038 and the Region SUD contract 2018-06085. This work also benefitted from the MATRAC research project sponsored by ANR-ASTRID under contract ANR-18-ASTR-0002.

Appendix A Studying CSASP probe flow rates

CSASP systems have been used in a variety of conditions and have been shown to be reliable (Frick & Hoppel, 2000; Savelyev et al., 2014; Petelski et al., 2014). An isokinetic inlet and a fan maintain a constant flow rate, and are essential components for the rerouting of the sampled particles with a limited pertubation by the probes.During the MATE19 deployment at the Luminy facility this was verified for the CSASP-100-HV-ER and CSASP-200 probes, in wind speeds ranging from 0 to 15 m s^{-1}. A hot film wind sensor (E+E Elektronik, Langwiesen, Austria) was inserted through the side of a tube, printed to match the exact size of the probe outlets. The output flow rate of the probes was calculated from the probe outlet wind speeds (cf Fig. A.1). Figures A1a and A1b present the velocities measured out of the CSASP-

t to

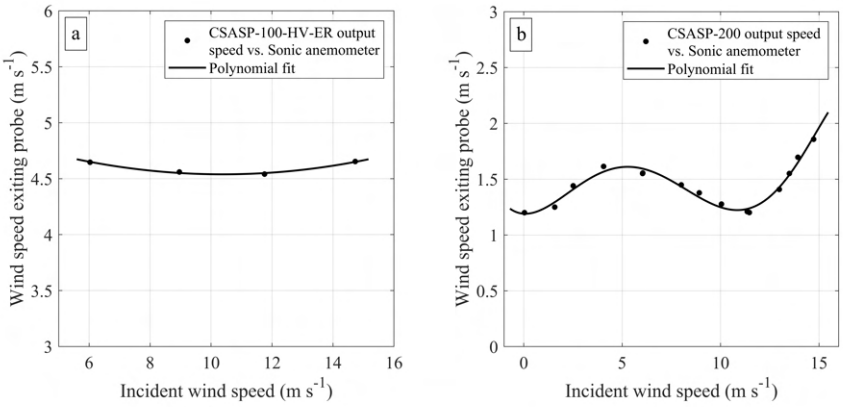

Figure A1. Measurements of wind velocities exiting probes as a function of incident wind speed.

As shown in Fig. A.1a, the wind had little influence on the CSASP-100-HV-ER. Values were found to match factory settings. The CSASP-200 showed a non-linear response to the incident wind. The current hypothesis is that, despite its isokinetic inlet, the CSAPS-200 is subject to flow distortion in high winds due to accumulated static pressure. This is consistent with the higher sensitivity of the flow-regulating fan system in the CSASP-200 to static pressure fluctuations, as indicated by the manufacturer. This result highlights some of the many intricacies of aerosol measurements, and the good characterization of the volume of air sampled by the probe.

Appendix B Studying CSASP probe flow rates

In previous work (Bruch et al., 2021), sea spray droplets size distributions are described by a normal shape. Some authors formulate size distributions as the sum of lognormal distributions. Such lognormal distributions can be written for a number of modes m

$$\frac{dF}{dln(r)} = \sum_{i=1}^{m} \frac{F_i}{\sqrt{2\pi} ln\sigma_i} exp(-\frac{1}{2}\frac{ln^2\frac{r}{r_i}}{ln^2\sigma_i}) \tag{B1}$$

where r_g, σ_g and F_i are the median radius, standard deviation and the size-dependent generation flux for a given mode i. r is the radius increment.

In the present study, for conformity with the Meso-NH aerosol module, B21A and B21B SSGFs are re-formulated as lognormal distributions. Upon comparison, no significant difference is observed between the resulting normal and lognormal shapes. The corresponding parameters are given in Table B1.

Table B1. Lognormal parameters for the two laboratory SSGFs.

i	σ_i	μ_i	$F_i(\frac{u*^3}{\nu_a g}\langle S^2\rangle)$	$F_i(\langle S^2\rangle)$
1	1.55	2.5	$4.76\times10^{1}\times(\frac{u*^3}{\nu_a g}\langle S^2\rangle)^{0.92}$	$5.38\times10^{6}\times(\langle S^2\rangle)^{2.45}$
2	1.8	7	$1.69\times(\frac{u*^3}{\nu_a g}\langle S^2\rangle)^{1.41}$	$1.94\times10^{6}\times(\langle S^2\rangle)^{2.3}$
3	2.1	25	$4.5\times10^{-1}\times(\frac{u*^3}{\nu_a g}\langle S^2\rangle)^{1.11}$	$1.31\times10^{5}\times(\langle S^2\rangle)^{2.39}$

Video Supplement

A video supplement is located at https://www.youtube.com/watch?v=IRrRdmycfdY

References

Amante, C., & Eakins, B. W. (2009). Etopo1 arc-minute global relief model: procedures, data sources and analysis.

Anctil, F., & Donelan, M. (1996). Air–water momentum flux observations over shoaling waves. *Journal of physical oceanography*, *26*(7), 1344–1353.

Andreas, E. L. (1992). Sea spray and the turbulent air-sea heat fluxes. *J Geophys Res: Oceans*, *97*(C7), 11429-11441. Retrieved from `https://agupubs.onlinelibrary.wiley.com/doi/abs/10.1029/92JC00876` doi: 10.1029/92JC00876

Andreas, E. L. (1998). A new sea spray generation function for wind speeds up to 32 m/s. *J Phys Ocean*, *28*(11), 2175-2184. Retrieved from `https://doi.org/10.1175/1520-0485(1998)028<2175:ANSSGF>2.0.CO;2` doi: 10.1175/1520-0485(1998)028<2175:ANSSGF>2.0.CO;2

Andreas, E. L. (2004). Spray stress revisited. *Journal of physical oceanography*, *34*(6), 1429–1440.

Andreas, E. L., & Emanuel, K. A. (2001). Effects of sea spray on tropical cyclone intensity. *Journal of the atmospheric sciences*, *58*(24), 3741–3751.

Andreas, E. L., Jones, K. F., & Fairall, C. W. (2010). Production velocity of sea spray droplets. *J of Geophys Res: Oceans*, *115*(C12).

Augustin, P., Billet, S., Crumeyrolle, S., Deboudt, K., Dieudonné, E., Flament, P., ... others (2020). Impact of sea breeze dynamics on atmospheric pollutants and their toxicity in industrial and urban coastal environments. *Remote Sensing*, *12*(4), 648.

Bao, J.-W., Fairall, C. W., Michelson, S., & Bianco, L. (2011). Parameterizations of sea-spray impact on the air–sea momentum and heat fluxes. *Monthly Weather Review*, *139*(12), 3781–3797.

Bianco, L., Bao, J.-W., Fairall, C., & Michelson, S. (2011). Impact of sea-spray on the atmospheric surface layer. *Boundary-layer meteorology*, *140*(3), 361–381.

Blanchard, D. C. (1963). The electrification of the atmosphere by particles from bubbles in the sea. *Prog Ocean*, *1*, 73–202.

Bock, E. J., Hara, T., Frew, N. M., & McGillis, W. R. (1999). Relationship between air-sea gas transfer and short wind waves. *J Geophys Res: Oceans*, *104*(C11), 25821–25831.

Boucher, O., Randall, D., Artaxo, P., Bretherton, C., Feingold, G., Forster, P., ... others (2013). Clouds and aerosols. In *Climate change 2013: the physical science basis. contribution of working group i to the fifth assessment report of the intergovernmental panel on climate change* (pp. 571–657). Cambridge University Press.

Bourras, D., Weill, A., Caniaux, G., Eymard, L., Bourlès, B., Letourneur, S., ... others (2009). Turbulent air-sea fluxes in the gulf of guinea during the amma experiment. *Journal of Geophysical Research: Oceans*, *114*(C4).

Bradley, E. F. (1968). A micrometeorological study of velocity profiles and surface drag in the region modified by a change in surface roughness. *Quarterly Journal of the Royal Meteorological Society*, *94*(401), 361–379.

Bréon, F., & Henriot, N. (2006). Spaceborne observations of ocean glint reflectance and modeling of wave slope distributions. *Journal of Geophysical Research: Oceans*, *111*(C6).

Bruch, W. (2022). *études expérimentales et numériques de la génération et du transport des aérosols marins, ainsi que des conséquences sur les propriétés de la couche limite atmosphérique marine* (Unpublished doctoral dissertation). Université de Toulon.

Bruch, W., Piazzola, J., Branger, H., van Eijk, A. M., Luneau, C., Bourras, D., & Tedeschi, G. (2021). Sea-spray-generation dependence on wind and wave combinations: A laboratory study. *Boundary-Layer Meteorology*, 1–29.

Carruthers, D., & Choularton, T. (1986). The microstructure of hill cap clouds. *Quarterly Journal of the Royal Meteorological Society*, *112*(471), 113–129.

Chalikov, D., & Rainchik, S. (2011). Coupled numerical modelling of wind and waves and the theory of the wave boundary layer. *Boundary-layer meteorology*, *138*(1), 1–41.

Chen, Y., Cheng, Y., Ma, N., Wolke, R., Nordmann, S., Schüttauf, S., ... others (2016). Sea salt emission, transport and influence on size-segregated nitrate simulation: a case study in northwestern europe by WRF-Chem. *Atmos Chem and Phys*, *16*(18), 12081–12097.

Cox, C., & Munk, W. (1954). Measurement of the roughness of the sea surface from photographs of the sun's glitter. *Josa*, *44*(11), 838–850.

de Leeuw, G., Andreas, E. L., Anguelova, M. D., Fairall, C., Lewis, E. R., O'Dowd, C., ... Schwartz, S. E. (2011). Production flux of sea spray aerosol. *Rev of Geophys*, *49*(2).

Donelan, M. A. (2001). A nonlinear dissipation function due to wave breaking. In *Proc. ecmwf workshop on ocean wave forecasting* (pp. 87–94).

Dupuis, H., Guerin, C., Hauser, D., Weill, A., Nacass, P., Drennan, W., ... Graber, H. (2003). Impact of flow distortion corrections on turbulent fluxes estimated by the inertial dissipation method during the fetch experiment on r/v l'atalante. *Journal of Geophysical Research: Oceans*, *108*(C3).

Edson, J. B., Jampana, V., Weller, R. A., Bigorre, S. P., Plueddemann, A. J., Fairall, C. W., ... Hersbach, H. (2013). On the exchange of momentum over the open ocean. *Journal of Physical Oceanography*, *43*(8), 1589–1610.

Elfouhaily, T., Chapron, B., Katsaros, K., & Vandemark, D. (1997). A unified directional spectrum for long and short wind-driven waves. *J Geophys Res: Oceans*, *102*(C7), 15781–15796.

Fairall, C., Banner, M., Peirson, W., Asher, W., & Morison, R. (2009). Investigation of the physical scaling of sea spray spume droplet production. *J Geophys Res: Oceans*, *114*(C10).

Fairall, C., & Davidson, K. (1986). Dynamics and modeling of aerosols in the marine atmospheric boundary layer. In *Ocean white* (pp. 195–208). Springer.

Fairall, C., Kepert, J., & Holland, G. (1994). The effect of sea spray on surface energy transports over the ocean. *Global Atmos. Ocean Syst*, *2*(2-3), 121–142.

Fairall, C., Pezoa, S., Moran, K., & Wolfe, D. (2014). An observation of sea-spray microphysics by airborne doppler radar. *Geophysical Research Letters*, *41*(10), 3658–3665.

Forestieri, S., Moore, K., Martinez Borrero, R., Wang, A., Stokes, M., & Cappa, C. (2018). Temperature and composition dependence of sea spray aerosol production. *Geophysical Research Letters*, *45*(14), 7218–7225.

Frick, G., & Hoppel, W. (2000). Airship measurements of ship's exhaust plumes and their effect on marine boundary layer clouds. *J Atmos Sci*, *57*(16), 2625–2648.

Garratt, J. (1990). The internal boundary layer—a review. *Boundary-layer meteorology*, *50*(1), 171–203.

Glover, D. M., Frew, N. M., & McCue, S. J. (2007). Air–sea gas transfer velocity estimates from the jason-1 and topex altimeters: Prospects for a long-term global time series. *Journal of Marine Systems*, *66*(1-4), 173–181.

Grare, L., Statom, N. M., Pizzo, N., & Lenain, L. (2021). Instrumented wave gliders for air-sea interaction and upper ocean research. *Frontiers in Marine Science*, 888.

Grini, A., Tulet, P., & Gomes, L. (2006). Dusty weather forecasts using the mesonh mesoscale atmospheric model. *Journal of Geophysical Research: Atmospheres*, *111*(D19).

Harb, C., & Foroutan, H. (2022). Experimental development of a lake spray source function and its model implementation for great lakes surface emissions. *Atmospheric Chemistry and Physics Discussions*, 1–32.

Hasselmann, K., Barnett, T., Bouws, E., Carlson, H., Cartwright, D., Enke, K., ... others (1973). Measurements of wind-wave growth and swell decay during the joint north sea wave project (JONSWAP). *Ergänzungsheft 8-12*.

Hauser, D., Caudal, G., Guimbard, S., & Mouche, A. (2008). A study of the slope probability density function of the ocean waves from radar observations. *Journal of Geophysical Research: Oceans*, *113*(C2).

Hoarau, T., Barthe, C., Tulet, P., Claeys, M., Pinty, J.-P., Bousquet, O., ... Vié, B. (2018). Impact of the generation and activation of sea salt aerosols on the evolution of tropical cyclone dumile. *Journal of Geophysical Research: Atmospheres*, *123*(16), 8813–8831.

Iida, N., Toba, Y., & Chaen, M. (1992). A new expression for the production rate of sea water droplets on the sea surface. *J Ocean*, *48*(4), 439–460.

Jacobson, M. Z. (2001). Global direct radiative forcing due to multicomponent anthropogenic and natural aerosols. *Journal of Geophysical Research: Atmospheres*, *106*(D2), 1551–1568.

Jaenicke, R. (1984). *Physical aspects of atmospheric aerosol. In: Georgii, H. Jaeschke, W (eds) Chemistry of the unpolluted and polluted troposphere (pp. 341-373).* Springer, Dordrecht.

Jähne, B., & Riemer, K. S. (1990). Two-dimensional wave number spectra of small-scale water surface waves. *J Geophys Res: Oceans*, *95*(C7), 11531–11546.

Johansson, J. H., Salter, M. E., Navarro, J. A., Leck, C., Nilsson, E. D., & Cousins, I. T. (2019). Global transport of perfluoroalkyl acids via sea spray aerosol. *Environ Sci: Proc & Impacts*, *21*(4), 635–649.

Katoshevski, D., Nenes, A., & Seinfeld, J. H. (1999). A study of processes that govern the maintenance of aerosols in the marine boundary layer. *Journal of Aerosol Science*, *30*(4), 503–532.

Komen, G. J., Cavaleri, L., Donelan, M., Hasselmann, K., Hasselmann, S., & Janssen, P. (1996). *Dynamics and modelling of ocean waves*.

Kudryavtsev, V., Makin, V., & Chapron, B. (1999). Coupled sea surface-atmosphere model: 2. spectrum of short wind waves. *Journal of Geophysical Research: Oceans*, *104*(C4), 7625–7639.

Lac, C., Chaboureau, J.-P., Masson, V., Pinty, J.-P., Tulet, P., Escobar, J., ... others (2018). Overview of the meso-nh model version 5.4 and its applications. *Geoscientific Model Development*, *11*(5), 1929–1969.

Laussac, S., Piazzola, J., Tedeschi, G., Yohia, C., Canepa, E., Rizza, U., & Van Eijk, A. (2018). Development of a fetch dependent sea-spray source function using aerosol concentration measurements in the north-western mediterranean. *Atmos Environ*, *193*, 177–189.

Lenain, L., & Melville, W. K. (2017). Evidence of sea-state dependence of aerosol concentration in the marine atmospheric boundary layer. *J Phys Ocean*, *47*(1), 69–84.

Lenain, L., Statom, N. M., & Melville, W. K. (2019). Airborne measurements of surface wind and slope statistics over the ocean. *J Phys Ocean*, *49*(11), 2799–2814.

Lighthill, J. (1999). Ocean spray and the thermodynamics of tropical cyclones. *Journal of engineering mathematics*, *35*(1), 11–42.

Liu, F., Mao, F., Rosenfeld, D., Pan, Z., Zang, L., Zhu, Y., ... Gong, W. (2022). Opposing comparable large effects of fine aerosols and coarse sea spray on marine warm clouds. *Communications Earth & Environment*, *3*(1), 1–9.

Marechal, G., & de Marez, C. (2022). Variability of surface gravity wave field over a realistic cyclonic eddy. *Ocean Science*, *18*(5), 1275–1292.

Mårtensson, E., Nilsson, E., de Leeuw, G., Cohen, L., & Hansson, H.-C. (2003). Laboratory simulations and parameterization of the primary marine aerosol production. *J Geophys Res: Atmos*, *108*(D9).

Masson, V., Le Moigne, P., Martin, E., Faroux, S., Alias, A., Alkama, R., ... others (2013). The surfexv7. 2 land and ocean surface platform for coupled or offline simulation of earth surface variables and fluxes. *Geoscientific Model Development*, *6*(4), 929–960.

Mehta, S., Ortiz-Suslow, D. G., Smith, A., & Haus, B. (2019). A laboratory investigation of spume generation in high winds for fresh and seawater. *J Geophys Res: Atmos*, *124*(21), 11297–11312.

Monahan, E., Davidson, K., & Spiel, D. (1982). Whitecap aerosol productivity deduced from simulation tank measurements. *Journal of Geophysical Research: Oceans*, *87*(C11), 8898–8904.

Monahan, E., Spiel, D., & Davidson, K. (1986). A model of marine aerosol generation via whitecaps and wave disruption. In *Oceanic whitecaps* (pp. 167–174). Springer.

Monahan, E. C., & Muircheartaigh, I. (1980). Optimal power-law description of oceanic whitecap coverage dependence on wind speed. *J Phys Ocean*, *10*(12), 2094–2099.

Munk, W. (2009). An inconvenient sea truth: Spread, steepness, and skewness of surface slopes. *Ann Rev Mar Sci*, *1*, 377–415.

Neumann, D., Matthias, V., Bieser, J., Aulinger, A., & Quante, M. (2016). A comparison of sea salt emission parameterizations in northwestern europe using a chemistry transport model setup. *Atmos Chem and Phys*, *16*, 9905–9933.

Nilsson, E. D., Hultin, K. A., Mårtensson, E. M., Markuszewski, P., Rosman, K., & Krejci, R. (2021). Baltic sea spray emissions: In situ eddy covariance fluxes vs. simulated tank sea spray. *Atmosphere*, *12*(2), 274.

Ovadnevaite, J., de Leeuw, G., Ceburnis, D., Monahan, C., Partanen, A.-I., Korhonen, H., ... others (2014). A sea spray aerosol flux parameterization encapsulating wave state. *Atmos Chem and Phys*, *14*(4), 1837.

Petelski, T., Markuszewski, P., Makuch, P., Jankowski, A., & Rozwadowska, A. (2014). Studies of vertical coarse aerosol fluxes in the boundary layer over the baltic sea. *Oceanogr*, *56*(4), 697–710.

Pianezze, J., Barthe, C., Bielli, S., Tulet, P., Jullien, S., Cambon, G., ... Cordier, E. (2018). A new coupled ocean-waves-atmosphere model designed for tropical storm studies: example of tropical cyclone Bejisa (2013–2014) in the South-West Indian Ocean. *J Adv Mod Earth Sys*, *10*(3), 801–825.

Piazzola, J., Bruch, W., Desnues, C., Parent, P., Yohia, C., & Canepa, E. (2021). Influence of meteorological conditions and aerosol properties on the covid-19 contamination of the population in coastal and continental areas in france: Study of offshore and onshore winds. *Atmos*, *12*(4), 523.

Piazzola, J., Forget, P., Lafon, C., & Despiau, S. (2009). Spatial variation of sea-spray fluxes over a mediterranean coastal zone using a sea-state model. *Boundary-Layer Meteorol*, *132*(1), 167–183.

Plant, W. J. (1982). A relationship between wind stress and wave slope. *J Geophys Res: Oceans*, *87*(C3), 1961–1967.

Ramanathan, V., Crutzen, P. J., Lelieveld, J., Mitra, A., Althausen, D., Anderson, J., ... others (2001). Indian ocean experiment: An integrated analysis of the climate forcing and effects of the great indo-asian haze. *Journal of Geophysical Research: Atmospheres*, *106*(D22), 28371–28398.

Rastigejev, Y., & Suslov, S. A. (2019). Effect of evaporating sea spray on heat fluxes in a marine atmospheric boundary layer. *Journal of Physical Oceanography*, *49*(7), 1927–1948.

Rastigejev, Y., & Suslov, S. A. (2022). Investigation of sea spray effect on the vertical momentum transport using an eulerian multifluid-type model. *Journal of Physical Oceanography*, *52*(1), 99–117.

Rastigejev, Y., Suslov, S. A., & Lin, Y.-L. (2011). Effect of ocean spray on vertical momentum transport under high-wind conditions. *Boundary-layer meteorology*, *141*(1), 1–20.

Regayre, L. A., Schmale, J., Johnson, J. S., Tatzelt, C., Baccarini, A., Henning, S., ... others (2020). The value of remote marine aerosol measurements for constraining radiative forcing uncertainty. *Atmospheric Chemistry and Physics*, *20*(16), 10063–10072.

Richter, D. H., & Sullivan, P. P. (2014). The sea spray contribution to sensible heat flux. *Journal of the Atmospheric Sciences*, *71*(2), 640–654.

Rogowski, P., Merrifield, S., Collins, C., Hesser, T., Ho, A., Bucciarelli, R., ... Terrill, E. (2021). Performance assessments of hurricane wave hindcasts. *Journal of Marine Science and Engineering*, *9*(7), 690.

Romero, L., Lenain, L., & Melville, W. K. (2017). Observations of surface wave–current interaction. *J Phys Ocean*, *47*(3), 615–632.

Romero, L., & Lubana, K. (2022). On the bimodality of the wind-wave spectrum: Mean-squared-slopes and azimuthal overlap integral. *Journal of Physical Oceanography*.

Saliba, G., Chen, C.-L., Lewis, S., Russell, L. M., Rivellini, L.-H., Lee, A. K., ... others (2019). Factors driving the seasonal and hourly variability of sea-spray aerosol number in the north atlantic. *Proceedings of the National Academy of Sciences*, *116*(41), 20309–20314.

Sauvage, C., Lebeaupin Brossier, C., & Bouin, M.-N. (2021). Towards kilometer-scale ocean-atmosphere-wave coupled forecast: a case study on a mediter-

ranean heavy precipitation event. *Atmospheric Chemistry and Physics Discussions*, 1–45.

Savelyev, I., Anguelova, M., Frick, G., Dowgiallo, D., Hwang, P., Caffrey, P., & Bobak, J. (2014). On direct passive microwave remote sensing of sea spray aerosol production. *Atmos Chem Phys*, *14*(21), 11611.

Seinfeld, J. H., & Pandis, S. N. (1997). Atmospheric chemistry and physics. *S45*, *1356*.

Sellegri, K., O'Dowd, C., Yoon, Y., Jennings, S., & de Leeuw, G. (2006). Surfactants and submicron sea spray generation. *J Geophys Res: Atmos*, *111*(D22).

Slinn, W., Hasse, L., Hicks, B., Hogan, A., Lal, D., Liss, P., ... Vittori, O. (1978). Some aspects of the transfer of atmospheric trace constituents past the air-sea interface. *Atmospheric Environment (1967)*, *12*(11), 2055–2087.

Slinn, W. G. N. (1983). Air-to-sea transfer of particles. In *Air-sea exchange of gases and particles* (pp. 299–405). Springer.

Smith, M., Park, P., & Consterdine, I. (1993). Marine aerosol concentrations and estimated fluxes over the sea. *Q J R Meteorol Soc*, *119*(512), 809–824.

Soloviev, A., & Lukas, R. (2010). Effects of bubbles and sea spray on air–sea exchange in hurricane conditions. *Boundary-layer meteorology*, *136*(3), 365–376.

Spiel, D. E. (1994). The sizes of the jet drops produced by air bubbles bursting on sea-and fresh-water surfaces. *Tellus B: Chem Phys Meteorol*, *46*(4), 325–338.

Sroka, S., & Emanuel, K. (2021). A review of parameterizations for enthalpy and momentum fluxes from sea spray in tropical cyclones. *Journal of Physical Oceanography*.

Stokes, G. G. (1880). Supplement to a paper on the theory of oscillatory waves. *Math Phys Pap*, *1*(314-326), 14.

Taylor, P. K., & Yelland, M. J. (2001). The dependence of sea surface roughness on the height and steepness of the waves. *Journal of physical oceanography*, *31*(2), 572–590.

Tedeschi, G., & Piazzola, J. (2011). Development of a 2d marine aerosol transport model: Application to the influence of thermal stability in the marine atmospheric boundary layer. *Atmos Res*, *101*(469–479), 10.

Troitskaya, Y., Kandaurov, A., Ermakova, O., Kozlov, D., Sergeev, D., & Zilitinkevich, S. (2018). The "bag breakup" spume droplet generation mechanism at high winds. Part I: Spray generation function. *J Phys Ocean*, *48*(9), 2167–2188.

Tsyro, S., Aas, W., Soares, J., Sofiev, M., Berge, H., & Spindler, G. (2011). Modelling of sea salt concentrations over Europe: key uncertainties and comparison with observations. *Atmos Chem and Phys*, *11*(20), 10367–10388.

Tulet, P., Crahan-Kaku, K., Leriche, M., Aouizerats, B., & Crumeyrolle, S. (2010). Mixing of dust aerosols into a mesoscale convective system: Generation, filtering and possible feedbacks on ice anvils. *Atmospheric Research*, *96*(2-3), 302–314.

Tulet, P., Crassier, V., Cousin, F., Suhre, K., & Rosset, R. (2005). Orilam, a three-moment lognormal aerosol scheme for mesoscale atmospheric model: Online coupling into the meso-nh-c model and validation on the escompte campaign. *Journal of Geophysical Research: Atmospheres*, *110*(D18).

Tulet, P., Crassier, V., Solmon, F., Guedalia, D., & Rosset, R. (2003). Description of the mesoscale nonhydrostatic chemistry model and application to a transboundary pollution episode between northern france and southern england. *Journal of Geophysical Research: Atmospheres*, *108*(D1), ACH–5.

van Eijk, A., Kusmierczyk-Michulec, J., Francius, M., Tedeschi, G., Piazzola, J., Merritt, D., & Fontana, J. (2011). Sea-spray aerosol particles generated in the surf zone. *Journal of Geophysical Research: Atmospheres*, *116*(D19).

Veron, F. (2015). Ocean spray. *Ann Rev Fluid Mech*, *47*, 507–538.

Veron, F., Hopkins, C., Harrison, E., & Mueller, J. (2012). Sea spray spume droplet production in high wind speeds. *Geophys Res Lett*, *39*(16).

Veron, F., & Mieussens, L. (2020). An eulerian model for sea spray transport and evaporation. *Journal of Fluid Mechanics*, *897*.

Vié, B., Pinty, J.-P., Berthet, S., & Leriche, M. (2016). Lima (v1. 0): A quasi two-moment microphysical scheme driven by a multimodal population of cloud condensation and ice freezing nuclei. *Geoscientific Model Development*, *9*(2), 567–586.

Wang, Y., Lee, K.-H., Lin, Y., Levy, M., & Zhang, R. (2014). Distinct effects of anthropogenic aerosols on tropical cyclones. *Nature Climate Change*, *4*(5), 368–373.

Wentz, F. J. (1976). Cox and munk's sea surface slope variance. *Geophysical Research Letters*, *81*, 1607–1608.

Wu, J. (1972). Sea-surface slope and equilibrium wind-wave spectra. *The Physics of Fluids*, *15*(5), 741–747.

Xu, X., Voermans, J. J., Ma, H., Guan, C., & Babanin, A. V. (2021). A wind–wave-dependent sea spray volume flux model based on field experiments. *Journal of Marine Science and Engineering*, *9*(11), 1168.

Yoon, Y., Ceburnis, D., Cavalli, F., Jourdan, O., Putaud, J., Facchini, M., ... others (2007). Seasonal characteristics of the physicochemical properties of north atlantic marine atmospheric aerosols. *J Geophys Res: Atmos*, *112*(D4).

Zhao, B., Qiao, F., Cavaleri, L., Wang, G., Bertotti, L., & Liu, L. (2017). Sensitivity of typhoon modeling to surface waves and rainfall. *Journal of Geophysical Research: Oceans*, *122*(3), 1702–1723.

Zhao, D., Toba, Y., Sugioka, K.-i., & Komori, S. (2006). New sea spray generation function for spume droplets. *Journal of Geophysical Research: Oceans*, *111*(C2).